

Weak Coupling Theory of Magic-Angle Twisted Bilayer Graphene

Jihang Zhu,^{1,2} Iacopo Torre,³ Marco Polini,^{4,5,3} and Allan H. MacDonald⁶

¹Condensed Matter Theory Center and Joint Quantum Institute,

Department of Physics, University of Maryland, College Park, Maryland 20742, USA

²Max Planck Institute for the Physics of Complex Systems, 01187 Dresden, Germany

³ICFO-Institut de Ciències Fotòniques, The Barcelona Institute of Science and Technology,
Av. Carl Friedrich Gauss 3, 08860 Castelldefels (Barcelona), Spain

⁴Dipartimento di Fisica dell'Università di Pisa, Largo Bruno Pontecorvo 3, I-56127 Pisa, Italy

⁵Istituto Italiano di Tecnologia, Graphene Labs, Via Morego 30, I-16163 Genova, Italy

⁶Physics Department, University of Texas at Austin, Austin TX 78712 USA

Strong correlations occur in magic-angle twisted bilayer graphene (MATBG) when the octet of flat moiré minibands centered on charge neutrality (CN) is partially occupied. The octet consists of a single valence band and a single conduction band for each of four degenerate spin-valley flavors. Motivated by the importance of Hartree electrostatic interactions in determining the filling-factor dependent band structure, we use a time-dependent Hartree approximation to gain insight into electronic correlations. We find that the electronic compressibility is dominated by Hartree interactions, that paramagnetic states are stable over a range of density near CN, and that the dependence of energy on flavor polarization is strongly overestimated by mean-field theory.

Introduction— The energy bands of twisted bilayer graphene (TBG) have a four-fold spin-valley flavor degeneracy. As a magic twist angle near $\theta = 1^\circ$ is approached, the two sets of four-fold degenerate bands closest to the neutral system Fermi energy approach each other and narrow [1], converting graphene from a weakly-correlated Fermi liquid to a strongly correlated system [2–5] with a rich variety of competing states, including superconductors, insulating flavor ferromagnets, and metallic flavor ferromagnets. The ferromagnetism is reminiscent of but distinct from that exhibited by Bernal-stacked bilayer graphene in the quantum Hall regime [6–13] and is now clearly established [3, 5, 14–32] as a prominent part of the physics of MATBG. In contrast to the quantum Hall case, in which eight Landau bands are filled sequentially to minimize the exchange energy, MATBG ground states appear [33] not to have any broken symmetries for a range of filling factors near CN, and in broken symmetry states to keep the filling factors of partially occupied flavors ν_f inside an interval $(-\nu_h^*, \nu_e^*)$, where ν_h^* and ν_e^* are maximum hole and electron filling factors. ($\nu_f \equiv (N_f - M)/M$ where N_f is the number of flat band electrons with flavor f and M is the number of moiré cells in the system; $\nu = \sum_f \nu_f$.)

In this Letter, we address some unusual aspects of the correlation physics of MATBG from the weak-coupling point of view (one shot GW approximation). We find that the average compressibility is dominated by Hartree interactions, that unbroken symmetry states are stable over a range of density near CN, and that the dependence of energy on flavor polarization is strongly overestimated by mean-field theory. Below we first explain the technical details of our calculations and then discuss the relationship of our findings to those obtained using other approaches to MATBG interaction physics.

Moiré-Band Weak-coupling Theory— The one shot GW approximation, also known as the random phase approximation (RPA), is a perturbative method that accounts for dynamic screening of long-range Coulomb interactions. It is commonly used [34, 35] in *ab initio* electronic structure theory to under-

stand collective electronic behaviors, especially as probed by optical or photoemission spectroscopy. Although rigorously justified [36] only in weakly interacting systems, it has recently attracted interest [37] as a universal and accurate method for total energy calculations in many real materials, including [38] strongly correlated Mott insulators.

In this Letter we employ RPA theory to approximate the dependence of energy on the total band filling factor and on the partitioning of electrons between the four spin-valley flavors of MATBG. Because the number of electrons for each flavor is a good quantum number, we can approximate the magnetic energy landscape by adding exchange-correlation (xc) corrections E_{xc} to the self-consistent Hartree (SCH) energies of flavor polarized states. The RPA theory is motivated by the unusual property of MATBG, illustrated in Fig. 2 by plotting SCH bands at a series of band filling factors, that the band filling dependence of its total energy is dominated [39–43] by a Hartree mean-field contribution. The SCH energy increases rapidly as the flat bands are filled as shown in Fig. 1(c), and dominates the experimentally measured compressibility. The RPA accounts both for this energy, and for dynamic fluctuation corrections to it.

The xc correction to the SCH energy can be expressed [44], in terms of a coupling-constant integral of the pair correlation function. This quantity can in turn be related to the density response function by

$$E_{xc} = \frac{1}{2} \sum_{\mathbf{q}, \mathbf{g}} V_{\mathbf{q}+\mathbf{g}} \left[-\frac{1}{\pi} \int_0^1 d\lambda \int_0^\infty d\omega \chi^{\mathbf{gg}}(\mathbf{q}, i\omega; \lambda) - 1 \right], \quad (1)$$

where $V_{\mathbf{q}} = 2\pi e^2/q\epsilon_{\text{BN}}$ is the two-dimensional (2D) Coulomb interaction accounting for hexagonal boron nitride (hBN) dielectric screening with the dielectric constant chosen to be $\epsilon_{\text{BN}} = 5.1$ throughout the paper, \mathbf{q} is a wavevector in the moiré Brillouin zone (MBZ), \mathbf{g} is a moiré reciprocal lattice vector, and the prime on the sum excludes the $\mathbf{q} = \mathbf{g} = 0$ term which

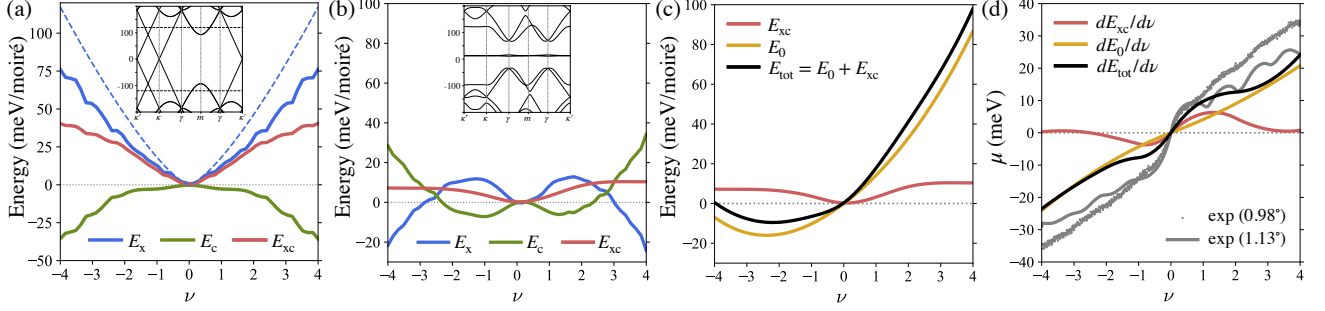


FIG. 1. Energies of paramagnetic states as a function of $\nu \in [-4, 4]$ for (a) a decoupled-bilayer and (b-d) 1.1° -TBG. (a-b) Exchange (E_x) and RPA correlation (E_c) energies as defined in Eqs. (4-5). The insets show the corresponding single-particle band structures. The black dashed lines in the inset of (a) mark the Fermi level for $\nu = \pm 4$. The blue dashed line in (a) is the exchange energy calculated using the approximate analytical expression Eq. (6). (c) The SCH energy E_0 [44] and the RPA total energy E_{tot} . (d) The calculated chemical potential $\mu = dE_{\text{tot}}/d\nu$ with its zero shifted to the chemical potential at $\nu = 0$. The grey dots (0.98°) and the grey line (1.13°) plot measured chemical potentials from Ref.[19]. All energies are given relative to CN with the zero of energy at the neutral system Fermi level.

contributes only a gate-geometry-dependent constant [44]. In Eq. (1) $\chi^{\mathbf{g}\mathbf{g}}$ is a diagonal matrix element of the density response function, which is a matrix in reciprocal lattice vectors because of system's discrete translational symmetry, and the frequency integration used to obtain equal time correlations has been rotated to the imaginary axis.

Equation (1) is formally exact. In RPA (time-dependent Hartree) we replace χ in Eq. (1) by

$$\begin{aligned} \chi(\lambda) &= \tilde{\chi}_H (1 - \lambda V \tilde{\chi}_H)^{-1} \\ &= \tilde{\chi}_H + \lambda \tilde{\chi}_H V \tilde{\chi}_H (1 - \lambda V \tilde{\chi}_H)^{-1}, \end{aligned} \quad (2)$$

where $\tilde{\chi}_H$ is the single-particle density response function calculated from the SCH bands [45], summing over independent

contributions from all four flavors:

$$\tilde{\chi}_H = \sum_{f=1}^4 \tilde{\chi}_H^f. \quad (3)$$

Possible improvements to this approximation are discussed later.

When inserted in Eq. (1), the second form for the right-hand-side of Eq. (2) separates the exchange energy E_x , the contribution that is first order in V , from the full fluctuation correction $E_{xc} \equiv E_x + E_c$, allowing us to carefully account for its subtly convergent frequency integral. After integrating over λ , the exchange energy can be rewritten in the standard Slater determinant form [44]:

$$E_x = -\frac{1}{2A} \sum_{\mathbf{q}, \mathbf{g}} V_{\mathbf{q}+\mathbf{g}} \sum_{\substack{f, \mathbf{k}, \alpha \\ \beta, \mathbf{g}_1, \mathbf{g}_2}} [\delta \bar{\rho}^f(\mathbf{k}) + 2\bar{\rho}^{0f}(\mathbf{k})]_{\alpha, \mathbf{g}_1; \beta, \mathbf{g}_2} \delta \rho_{\alpha, \mathbf{g}_1+\mathbf{g}; \beta, \mathbf{g}_2+\mathbf{g}}^f(\mathbf{k} + \mathbf{q}), \quad (4)$$

where $\delta \rho^f(\mathbf{k}) = \sum_n \left(\hat{z}_n(\mathbf{k}) \hat{z}_n^\dagger(\mathbf{k}) \Theta_{n\mathbf{k}} - \hat{z}_n^0(\mathbf{k}) \hat{z}_n^{0\dagger}(\mathbf{k}) \Theta_{n\mathbf{k}}^0 \right)$ is the density matrix projected to flavor f relative to that of a charge neutral decoupled bilayer, $\delta \bar{\rho}$ is the complex conjugate of the corresponding matrix element of $\delta \rho$, $\hat{z}_n(\mathbf{k})$ and $\hat{z}_n^0(\mathbf{k})$ are plane-wave representation SCH and neutral-decoupled-bilayer quasiparticle eigenvectors, and $\Theta_{n\mathbf{k}}$ and $\Theta_{n\mathbf{k}}^0$ are the corresponding occupation numbers. In Eq. (4) $\mathbf{g}, \mathbf{g}_1, \mathbf{g}_2$ are moiré reciprocal lattice vectors, \mathbf{k} and \mathbf{q} are momenta in MBZ, α and β are layer and sublattice indices and A is the area of the 2D system. Because of their negative energy seas, continuum models of graphene multilayers are able to determine total energies only up to a reference energy (per area) that is a linear functions of electron density, $\varepsilon_{\text{ref}} = \varepsilon_0 + \mu_0 n$; Eq. (4) chooses the zero of energy ε_0 to be the energy per area of neutral decoupled bilayers and the zero of chemical potential μ_0 to be the energy of states at the top of the decoupled bilayer valence

band. The integration over the coupling-constant λ in Eq. (1) can be performed analytically to yield the correlation energy [44]

$$E_c = \frac{1}{2\pi} \sum_{\mathbf{q}} \int_0^\infty d\omega \text{Tr} \left[\sqrt{\mathbf{V}} \tilde{\chi}_H \sqrt{\mathbf{V}} + \ln(1 - \sqrt{\mathbf{V}} \tilde{\chi}_H \sqrt{\mathbf{V}}) \right], \quad (5)$$

where \mathbf{V} and $\tilde{\chi}_H$ are matrices in reciprocal lattice vector with implicit \mathbf{q} and ω dependences. The correlation energy must be regularized by subtracting its value in unbroken symmetry states at CN; its contribution to the chemical potential at CN is close to zero because the models we study have approximate particle-hole symmetry.

Paramagnetic State Energy — We interpret our numerical results for the band filling ν dependence of the MATBG paramagnetic ground state energy (Fig. 1(b,c)) by comparing them

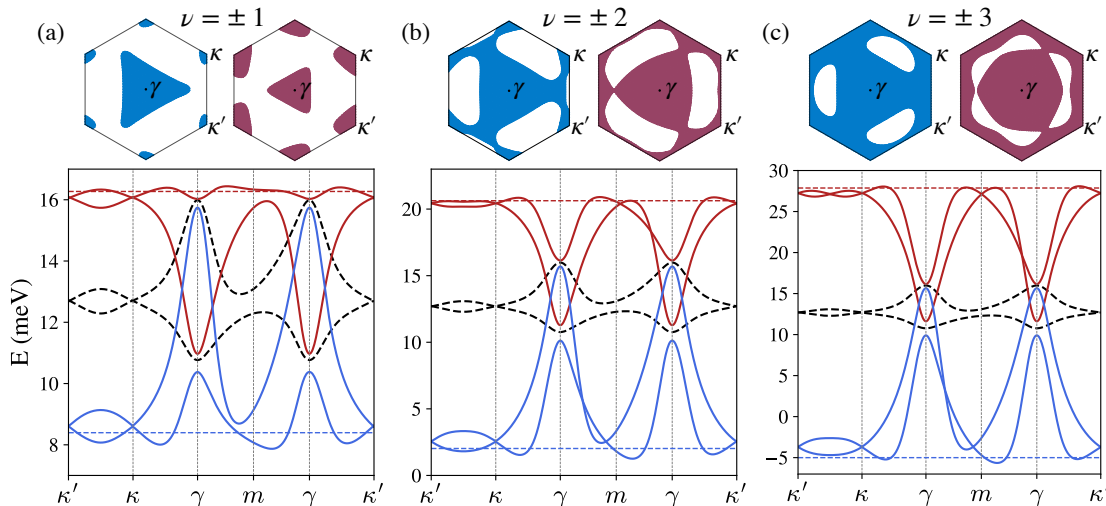


FIG. 2. The SCH paramagnetic state bands (colored lines) and the corresponding Fermi surfaces (shaded areas) at a series of ν values on hole-doped (blue) and electron-doped (red) sides. The black dashed line in each spectrum is the single-particle band structure and the colored dashed horizontal lines mark Fermi levels. At $\nu = -3$, the flat valence band is 1/4 full and the occupied states are those whose charge density is most peaked near minima of the external potential produced by remote band charges. At $\nu = -1$, the flat valence band is at 3/4 filling. Holes in the valence band remain near γ , which would be the valence band bottom if Hartree corrections were not included. Holes near γ are finally filled only around $\nu = -0.3$ (see Fig. 5 in SM III) as ν approaches zero and Hartree energies finally become small compared to band energies. The Fermi surfaces at filling factors $+\nu$ and $-\nu$ (for example $\nu = 2$ and $\nu = -2$) would be identical for any ν if the model had exact particle-hole symmetry. At filling factors away from $\nu = 0$, the SCH band width is dominated by the Hartree mean-field contribution.

with results for the decoupled bilayer [46] (Fig. 1(a)) calculated in exactly the same way. In both cases the exchange energy is positive at small $|\nu|$ because of [46] rapid changes in Bloch state spinors near the Dirac point. The blue dashed line in Fig. 1(a) is the exchange energy of an eight-Dirac-cone model [46]:

$$E_x^D = \frac{\alpha \hbar c}{24\pi} \frac{g}{\epsilon_{\text{BN}}} k_F^3 \ln\left(\frac{k_c}{k_F}\right) + \text{regular terms}, \quad (6)$$

where $g = 8$ and $k_F = (4\pi n/g)^{1/2}$. The exchange energy of MATBG is smaller than that of decoupled bilayers because of the dominant role of the Hartree potential in shaping occupied band states wavefunctions. In contrast to the decoupled bilayer case, MATBG correlation energies are low near CN, because that is where the phase space for low-energy particle-hole excitations within the flat band octet is the largest. The correlation energy is highest near $|\nu| = 4$ because the gaps between flat and remote bands suppress fluctuations. In our calculations there is a small particle-hole asymmetry in all properties, including the exchange and correlation energies, because we include non-local interlayer tunneling corrections [47] to the Bistritzer-MacDonald (BM) MATBG model [1, 44].

Because of the partial cancellation between exchange and correlation effects, discussed again below in connection with flavor ferromagnetism, the difference between MATBG and decoupled bilayers is dominated by the SCH energy [44] plotted in Fig. 1(c). The SCH energy is calculated relative to its value at CN, and its slope at CN is finite because the bare flat bands are centered around $\epsilon_{\text{fb}} \approx 12$ meV (see Fig. 2) in the non-local BM model we employ. The chemical potential μ , the energy to add a single-electron increases steadily

as the flat bands are filled mainly because of Hartree effects. We find that the chemical potential difference between full and empty flat bands is ~ 50 meV. When the bands are nearly empty, added electrons occupy regions in the moiré unit cell in which the mean-field potential from remote band electrons is most attractive. When the bands are nearly filled, on the other hand, it follows from approximate particle-hole symmetry that electrons occupy the same region but the Hartree mean-field potential is now repulsive.

In Fig. 1(d) we compare our results for the filling factor dependence of the chemical potential across the full range of flat band filling with experimental results published in Ref. [19]. The total shift in chemical potential is somewhat larger in experiment than in theory. Since the states near the full and empty flat band limit are not expected to be strongly correlated, we attribute this small discrepancy to weak mixing between flat and remote bands and small inaccuracies in the continuum model we employ. The most striking feature of these results is shared between theory and experiment, namely that the chemical potential increases approximately linearly with band filling factor [19, 20, 48, 49]. In MATBG experiments, structures do emerge at some filling factors that are thought to be due to first order flavor-symmetry breaking phase transitions at low temperatures, which we now address, and at higher temperatures to surviving local moment fluctuations [50].

Flat Band Flavor Ferromagnetism — The RPA energy calculation can be carried out for any set of flavor-dependent filling factors. Typical numerical results [51] are summarized in Fig. 3. The $\nu = 0$ polarized states in Fig. 3(c) have filling factor p for two flavors and filling factor $-p$ for the other two

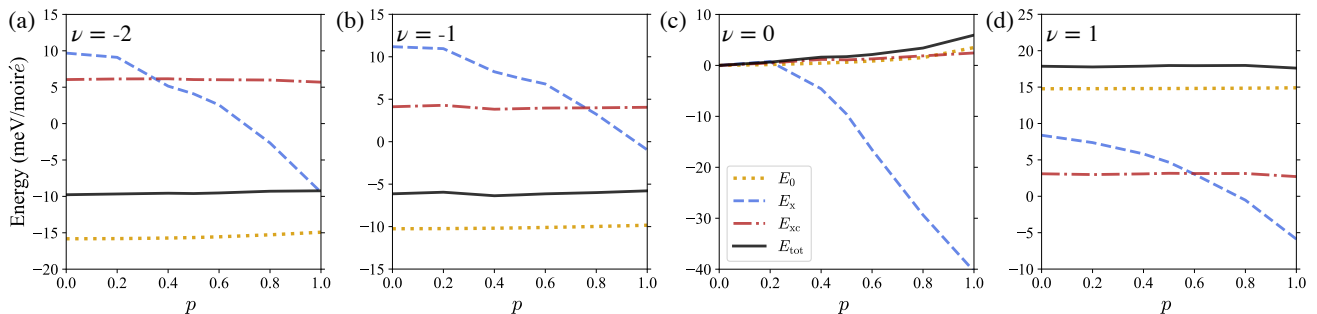


FIG. 3. SCH energy E_0 (yellow dotted lines), exchange energy E_x (blue dashed lines), exchange-correlation energy E_{xc} (red dash-dotted lines) and RPA total energy E_{tot} (black solid lines) as a function of polarization p at (a) $\nu = -2$, (b) $\nu = -1$, (c) $\nu = 0$ and (d) $\nu = 1$. p characterizes the degree of flavor polarization as explained in the main text. $p = 0$ corresponds to the paramagnetic state and $p = 1$ corresponds to full flavor polarization.

flavors. Increasing p shifts states from the valence bands of two flavors to the conduction bands of the other two flavors. Because of MATBG's approximate particle-hole symmetry, this polarization path does not strongly influence the charge density, which remains approximately uniform at this filling factor for all values of p , as illustrated in Figs. 13,14. The main point to notice is that fully polarized states are strongly favored by exchange energies, but this energy gain is almost perfectly cancelled by the correlation energy which strongly favors states in which each flavor is half filled. Similar results are obtained at other filling factors. The family of polarized states at $\nu = -2$ in Fig. 3(a) have filling factor $-(1+p)/2$ for two flavors and filling factor $-(1-p)/2$ for the other two flavors; increasing p shifts electrons between valence bands with different flavors and the charge density is non-uniform at all values of p . For $\nu = \pm 1$, the flavor polarization path illustrated in Fig. 3(b,d) is $\nu = \pm(1+3p)/4$ for one flavor and $\nu = \pm(1-p)/4$ for the remaining three flavors. The exchange energy gain upon polarization is again almost exactly cancelled by correlation, underscoring the dominance of the SCH energy. Once correlations are included the dependence of the SCH energy on p , which was judged to be insignificant in previous self-consistent Hartree-Fock [52] calculations, retains a role in the energy competition among different polarized states.

Within the RPA theory the cancellation between exchange and correlation for the polarization p dependence of the energy can be understood in terms of Eqs. (1-2). The p dependence of energy follows from that of $\tilde{\chi}_H$, and this lies mainly in the range of low-frequency fluctuations within the flat band where the important matrix elements of $V\tilde{\chi}_H$ are much larger than 1 so that $\chi(\lambda) \rightarrow V^{-1}$ (perfect screening), and the dependence of E_{xc} on polarization is lost. Physically, correlations are already strong even in the paramagnetic state and there is little left to gain by flavor ordering. Generally speaking, we find that the tendency toward flavor symmetry breaking is stronger at larger $|\nu|$ and stronger at positive ν than at negative ν , as summarized in Fig. 10, in agreement with most experiments [16, 19, 48, 53]. In addition we find that the difference in energy between polarized and paramagnetic states is drastically reduced by correlations from ~ 40 meV per moiré period to less than ~ 3

meV (Fig. 3(c)).

In MATBG broken C_2T symmetry opens up a gap between the conduction and valence bands. This type of broken symmetry within flavors is therefore common in mean-field calculations. In our RPA calculations we find, as summarized in Table II, that when C_2T symmetry is broken by adding a sublattice-dependent potential of the type produced by aligned hBN substrates, flavor ferromagnetism is favored at almost all filling factors including those proximate to CN. This finding aligns well with experimental evidence suggesting that hBN alignment tends to favor states with broken symmetries [14, 15, 54], including quantum anomalous Hall states at fractional flat band fillings [14].

The Magic-Angle Correlation Problem— In this Letter we have reported on the first RPA calculation for MATBG. The RPA weak-coupling approach has the advantage that it accounts for dynamic screening of long-range Coulomb interactions, but is less reliable than some other methods in accounting for short-distance correlations. Competing methods often require tight-binding models, which in the case of MATBG have the disadvantage that they require the introduction of additional bands [55] to compensate for fragile topology inherited from the isolated layer Dirac cones. Our theory establishes the crucial influence of correlations in compressible metallic states in expanding unbroken symmetry regions in the MATBG phase diagram. The RPA weak-coupling approach is also relevant for other moiré materials that exhibit strong correlations.

Our calculations include 146 remote valence and conduction bands per spin and flavor. Our calculations are consistent with experimental indications that flavor ferromagnetism is common in both insulating and metallic states when the MATBG flat bands are partially filled, less likely close to CN, and more likely at positive filling factors than at negative filling factors. The exchange energy gains that favor broken symmetry insulating ground states at integer ν , are comparable in size to correlation energy gains in closely competing metallic states with fewer or no broken symmetries. The resulting weak dependence of energy on magnetic state is consistent with small collective excitation energies of insulating states [56, 57] and

with strong coupling approaches [22, 58] that can be applied close to integer band fillings. Our calculations demonstrate that [44] fluctuations in remote bands do not generally play a central role in MATBG properties except in the cases of nearly empty and nearly full bands. This finding justifies the flat-band projection that is required to make non-perturbative finite-size numerical calculations [59–62] feasible. Perturbative calculations are approximate, but have the advantage that finite-size effects can be eliminated by taking dense momentum space grids; our calculations employ 432 k -points in the MBZ.

Our calculation results can be compared directly to experimental results for the chemical potential μ , which increases by ~ 50 meV as the flat bands are filled. This compares to a dependence of energy on flavor polarization that is typically ~ 3 meV per moiré cell. The positive compressibility we find, in agreement with experiment, for MATBG electrons contrasts with the well-known negative compressibility of strongly interacting two-dimensional electron gas systems [63, 64], and is associated with unusual properties of the projected flat-band Hilbert space. In MATBG models with exact particle-hole symmetry, the flat conduction and valence bands at the Fermi energy spatial structure within the moiré unit cell that precisely complements the total density of remote occupied bands, so that the total density is uniform. The increase in chemical potential with filling factor is associated with the property that the non-uniform density of the remote bands is first eliminated and then restored with the opposite sign as the flat bands are filled. We emphasize that unlike most calculations in the literature, which overstate dielectric screening to suppress interaction scales, all our results are obtained using a physically realistic hBN dielectric constant $\epsilon_{\text{BN}} = 5.1$ [44].

The MATBG correlation problem is extraordinarily challenging and the RPA theory, like other approaches, has limitations. Even though the flat band eigenstates have weak dispersion, their wavefunctions vary in a complex way across the MBZ. For this reason there is no simple Hubbard-like lattice model representation of the correlation problem. Aside from the fascinating low-temperature superconducting instability, two key higher energy issues still do not have definitive answers. i) What is the ground state at CN? Is it the $p = 0$ state of Fig. 3, which has no broken symmetries and strong correlations, or the $p = 1$ state, which is a single Slater determinant with analytically calculable excitations when remote band fluctuations are neglected? ii) What is the Fermi surface in the range of filling factors surrounding $\nu = 0$? Is it the γ centered Fermi surface of the $p = 1$ state or the κ, κ' centered Fermi surface of the $p = 0$ state? In either case how does the Fermi surface, at least as indicated by weak-field Hall measurements [47], manage to avoid Lifshitz transitions over such a broad range of filling factors $-1.8 \lesssim \nu \lesssim 0.9$ surrounding $\nu = 0$? For the first question we do not consider the weak-coupling answer (that $p = 0$ is favored) to be definitive, but it certainly demonstrates that the two states are competitive. The second question is especially troublesome if one imagines that the ground state near $\nu = 0$ is a doped $p = 1$ state in which the band degeneracies have been reduced from four to two and

Fermi surface areas must be correspondingly larger. The more likely option, in our view, is that the ground state near CN is an unpolarized state as predicted by RPA. Part of the motivation for this view is the absence of finite-temperature anomalies in experiment, which would signal a phase transition to a paramagnetic state — expected to be at least weakly first order in MATBG as in other itinerant electron magnets [65]. If so, there is no hint experimentally of the emergence between $\nu = 0$ and $|\nu| = 1$ of the self-consistent Hartree multi-pocket Fermi surface topology illustrated in Fig. 2. Future work should explain why this pocket does not appear (or alternately why its appearance does not influence transport), perhaps due to a refinement of the single-particle model which changes flat band wavefunctions [66–69], exchange interactions within the doped flat bands that stabilize κ, κ' centered surfaces, broken C_2T symmetry related to chiral model physics [22, 56, 70, 71] and intervalley exchange interactions that we have neglected [71–73]. Systematic studies of the evolution of MATBG properties with gate induced interlayer displacement fields could play a role in sorting this confusing landscape.

Acknowledgements— Work in Austin was supported by the U.S. Department of Energy, Office of Science, Basic Energy Sciences, under Award DE-SC0019481. M.P. is supported by the European Union’s Horizon 2020 research and innovation program under the grant agreement No. 881603 - GrapheneCore3 and the Marie Skłodowska-Curie grant agreement No. 873028 and by the MUR - Italian Minister of University and Research under the “Research projects of relevant national interest - PRIN 2020” - Project No. 2020JLZ52N, title “Light-matter interactions and the collective behavior of quantum 2D materials (q-LIMA)”. The authors acknowledge resources provided by the Texas Advanced Computing Center (TACC) at The University of Texas at Austin that have contributed to the research results reported in this paper.

-
- [1] R. Bistritzer and A. H. MacDonald, *Moiré bands in twisted double-layer graphene*, Proceedings of the National Academy of Sciences **108**, 12233 (2011).
 - [2] Y. Cao, V. Fatemi, S. Fang, K. Watanabe, T. Taniguchi, E. Kaxiras, and P. Jarillo-Herrero, *Unconventional superconductivity in magic-angle graphene superlattices*, Nature **556**, 43 (2018).
 - [3] Y. Cao, V. Fatemi, A. Demir, S. Fang, S. L. Tomarken, J. Y. Luo, J. D. Sanchez-Yamagishi, K. Watanabe, T. Taniguchi, E. Kaxiras, R. C. Ashoori, and P. Jarillo-Herrero, *Correlated insulator behaviour at half-filling in magic-angle graphene superlattices*, Nature **556**, 80 (2018).
 - [4] E. Y. Andrei and A. H. MacDonald, *Graphene bilayers with a twist*, Nature Materials **19**, 1265 (2020).
 - [5] L. Balents, C. R. Dean, D. K. Efetov, and A. F. Young, *Superconductivity and strong correlations in moiré flat bands*, Nature Physics **16**, 725 (2020).
 - [6] E. McCann and V. I. Fal’ko, *Landau-level degeneracy and quantum Hall effect in a graphite bilayer*, Phys. Rev. Lett. **96**, 086805 (2006).
 - [7] Y. Barlas, R. Côté, K. Nomura, and A. H. MacDonald, *Intralandau-level cyclotron resonance in bilayer graphene*, Phys.

- Rev. Lett. **101**, 097601 (2008).
- [8] R. Côté, J. Lambert, Y. Barlas, and A. H. MacDonald, *Orbital order in bilayer graphene at filling factor $\nu = -1$* , Phys. Rev. B **82**, 035445 (2010).
- [9] Y. Barlas, K. Yang, and A. H. MacDonald, *Quantum Hall effects in graphene-based two-dimensional electron systems*, Nanotechnology **23**, 052001 (2012).
- [10] B. E. Feldman, J. Martin, and A. Yacoby, *Broken-symmetry states and divergent resistance in suspended bilayer graphene*, Nature Physics **5**, 889 (2009).
- [11] J. Martin, B. E. Feldman, R. T. Weitz, M. T. Allen, and A. Yacoby, *Local compressibility measurements of correlated states in suspended bilayer graphene*, Phys. Rev. Lett. **105**, 256806 (2010).
- [12] R. T. Weitz, M. T. Allen, B. E. Feldman, J. Martin, and A. Yacoby, *Broken-symmetry states in doubly gated suspended bilayer graphene*, Science **330**, 812 (2010).
- [13] J. Jung, F. Zhang, and A. H. MacDonald, *Lattice theory of pseudospin ferromagnetism in bilayer graphene: Competing interaction-induced quantum Hall states*, Phys. Rev. B **83**, 115408 (2011).
- [14] M. Serlin, C. L. Tschirhart, H. Polshyn, Y. Zhang, J. Zhu, K. Watanabe, T. Taniguchi, L. Balents, and A. F. Young, *Intrinsic quantized anomalous Hall effect in a moiré heterostructure*, Science **367**, 900 (2020).
- [15] A. L. Sharpe, E. J. Fox, A. W. Barnard, J. Finney, K. Watanabe, T. Taniguchi, M. A. Kastner, and D. Goldhaber-Gordon, *Emergent ferromagnetism near three-quarters filling in twisted bilayer graphene*, Science **365**, 605 (2019).
- [16] P. Stepanov, M. Xie, T. Taniguchi, K. Watanabe, X. Lu, A. H. MacDonald, B. A. Bernevig, and D. K. Efetov, *Competing zero-field Chern insulators in superconducting twisted bilayer graphene*, Phys. Rev. Lett. **127**, 197701 (2021).
- [17] X. Lu, P. Stepanov, W. Yang, M. Xie, M. A. Aamir, I. Das, C. Urgell, K. Watanabe, T. Taniguchi, G. Zhang, A. Bachtold, A. H. MacDonald, and D. K. Efetov, *Superconductors, orbital magnets and correlated states in magic-angle bilayer graphene*, Nature **574**, 653 (2019).
- [18] H. Polshyn, J. Zhu, M. A. Kumar, Y. Zhang, F. Yang, C. L. Tschirhart, M. Serlin, K. Watanabe, T. Taniguchi, A. H. MacDonald, and A. F. Young, *Electrical switching of magnetic order in an orbital Chern insulator*, Nature **588**, 66 (2020).
- [19] U. Zondiner, A. Rozen, D. Rodan-Legrain, Y. Cao, R. Queiroz, T. Taniguchi, K. Watanabe, Y. Oreg, F. von Oppen, A. Stern, E. Berg, P. Jarillo-Herrero, and S. Ilani, *Cascade of phase transitions and dirac revivals in magic-angle graphene*, Nature **582**, 203 (2020).
- [20] D. Wong, K. P. Nuckolls, M. Oh, B. Lian, Y. Xie, S. Jeon, K. Watanabe, T. Taniguchi, B. A. Bernevig, and A. Yazdani, *Cascade of electronic transitions in magic-angle twisted bilayer graphene*, Nature **582**, 198 (2020).
- [21] I. Das, X. Lu, J. Herzog-Arbeitman, Z.-D. Song, K. Watanabe, T. Taniguchi, B. A. Bernevig, and D. K. Efetov, *Symmetry-broken Chern insulators and rashba-like landau-level crossings in magic-angle bilayer graphene*, Nature Physics **17**, 710 (2021).
- [22] E. Khalaf, S. Chatterjee, N. Bultinck, M. P. Zaletel, and A. Vishwanath, *Charged skyrmions and topological origin of superconductivity in magic-angle graphene*, Science Advances **7**, eabf5299 (2021).
- [23] Y. Saito, F. Yang, J. Ge, X. Liu, T. Taniguchi, K. Watanabe, J. I. A. Li, E. Berg, and A. F. Young, *Isospin pomeranchuk effect in twisted bilayer graphene*, Nature **592**, 220 (2021).
- [24] Y. Xie, A. T. Pierce, J. M. Park, D. E. Parker, E. Khalaf, P. Ledwith, Y. Cao, S. H. Lee, S. Chen, P. R. Forrester, K. Watanabe, T. Taniguchi, A. Vishwanath, P. Jarillo-Herrero, and A. Yacoby, *Fractional Chern insulators in magic-angle twisted bilayer graphene*, Nature **600**, 439 (2021).
- [25] S. Wu, Z. Zhang, K. Watanabe, T. Taniguchi, and E. Y. Andrei, *Chern insulators, van Hove singularities and topological flat bands in magic-angle twisted bilayer graphene*, Nature materials **20**, 488 (2021).
- [26] K. P. Nuckolls, M. Oh, D. Wong, B. Lian, K. Watanabe, T. Taniguchi, B. A. Bernevig, and A. Yazdani, *Strongly correlated Chern insulators in magic-angle twisted bilayer graphene*, Nature **588**, 610 (2020).
- [27] J. Kang and O. Vafek, *Strong coupling phases of partially filled twisted bilayer graphene narrow bands*, Phys. Rev. Lett. **122**, 246401 (2019).
- [28] B. Lian, Z.-D. Song, N. Regnault, D. K. Efetov, A. Yazdani, and B. A. Bernevig, *Twisted bilayer graphene. IV. exact insulator ground states and phase diagram*, Phys. Rev. B **103**, 205414 (2021).
- [29] X. Liu, G. Farahi, C.-L. Chiu, Z. Papic, K. Watanabe, T. Taniguchi, M. P. Zaletel, and A. Yazdani, *Visualizing broken symmetry and topological defects in a quantum Hall ferromagnet*, Science **375**, 321 (2022).
- [30] L. Wang, E.-M. Shih, A. Ghiotto, L. Xian, D. A. Rhodes, C. Tan, M. Claassen, D. M. Kennes, Y. Bai, B. Kim, K. Watanabe, T. Taniguchi, X. Zhu, J. Hone, A. Rubio, A. N. Pasupathy, and C. R. Dean, *Correlated electronic phases in twisted bilayer transition metal dichalcogenides*, Nature materials **19**, 861 (2020).
- [31] T. Wang, D. E. Parker, T. Soejima, J. Hauschild, S. Anand, N. Bultinck, and M. P. Zaletel, *Ground-state order in magic-angle graphene at filling $\nu = -3$: A full-scale density matrix renormalization group study*, Phys. Rev. B **108**, 235128 (2023).
- [32] J. Zhu, J.-J. Su, and A. H. MacDonald, *Voltage-controlled magnetic reversal in orbital Chern insulators*, Phys. Rev. Lett. **125**, 227702 (2020).
- [33] These statements are based on a minimal interpretation of measurements of electronic compressibility [19], tunneling spectroscopy [20] and weak-field Hall effects [47]. Other scenarios in which flavor symmetries are broken even at CN cannot be ruled out at present and are assumed in some theoretical work. Note that the cascades observed in the high-temperature compressibility experiment [23] (up to 100 K) are not indicative of ground state phase transitions. These high-temperature cascades may result from fluctuations of local moments, which can be explained by localized orbitals and the heavy fermion model [58, 74].
- [34] D. Golze, M. Dvorak, and P. Rinke, *The GW compendium: A practical guide to theoretical photoemission spectroscopy*, Frontiers in Chemistry **7** (2019), 10.3389/fchem.2019.00377.
- [35] J. Deslippe, G. Samsonidze, D. A. Strubbe, M. Jain, M. L. Cohen, and S. G. Louie, *Berkeleygw: A massively parallel computer package for the calculation of the quasiparticle and optical properties of materials and nanostructures*, Computer Physics Communications **183**, 1269 (2012).
- [36] M. Gell-Mann and K. A. Brueckner, *Correlation energy of an electron gas at high density*, Phys. Rev. **106**, 364 (1957).
- [37] T. Olsen and K. S. Thygesen, *Random phase approximation applied to solids, molecules, and graphene-metal interfaces: From Van der Waals to covalent bonding*, Phys. Rev. B **87**, 075111 (2013).
- [38] T. Olsen, *Assessing the performance of the random phase approximation for exchange and superexchange coupling constants in magnetic crystalline solids*, Phys. Rev. B **96**, 125143 (2017).
- [39] M. Xie and A. H. MacDonald, *Nature of the correlated insulator*

- states in twisted bilayer graphene, Phys. Rev. Lett. **124**, 097601 (2020).
- [40] F. Guinea and N. R. Walet, *Electrostatic effects, band distortions, and superconductivity in twisted graphene bilayers*, Proceedings of the National Academy of Sciences **115**, 13174 (2018).
- [41] T. Cea, N. R. Walet, and F. Guinea, *Electronic band structure and pinning of fermi energy to van Hove singularities in twisted bilayer graphene: A self-consistent approach*, Phys. Rev. B **100**, 205113 (2019).
- [42] L. Rademaker, D. A. Abanin, and P. Mellado, *Charge smoothening and band flattening due to Hartree corrections in twisted bilayer graphene*, Phys. Rev. B **100**, 205114 (2019).
- [43] T. Cea and F. Guinea, *Band structure and insulating states driven by coulomb interaction in twisted bilayer graphene*, Phys. Rev. B **102**, 045107 (2020).
- [44] See Supplemental Material (SM) at XXX for the derivation of Eq. (1) in SM II; the derivations of Eqs. (4-5) in SM VII; the definition of SCH energy E_0 in SM III; the expression of $\rho^{0f}(\mathbf{k})$ in Eq. (4) in SM VIII; details of MATBG model parameters that we use in this article in SM I; a detailed discussion on fluctuations in remote bands in SM IX; Fig. S12 for the energy dependence on dielectric constant ϵ_{BN} . The SM also contains Refs. [1, 22, 47, 66–69, 75–85].
- [45] P. Novelli, I. Torre, F. H. L. Koppens, F. Taddei, and M. Polini, *Optical and plasmonic properties of twisted bilayer graphene: Impact of interlayer tunneling asymmetry and ground-state charge inhomogeneity*, Phys. Rev. B **102**, 125403 (2020).
- [46] Y. Barlas, T. Pereg-Barnea, M. Polini, R. Asgari, and A. H. MacDonald, *Chirality and correlations in graphene*, Phys. Rev. Lett. **98**, 236601 (2007).
- [47] M. Xie and A. H. MacDonald, *Weak-field Hall resistivity and spin-valley flavor symmetry breaking in magic-angle twisted bilayer graphene*, Phys. Rev. Lett. **127**, 196401 (2021).
- [48] S. L. Tomarken, Y. Cao, A. Demir, K. Watanabe, T. Taniguchi, P. Jarillo-Herrero, and R. C. Ashoori, *Electronic compressibility of magic-angle graphene superlattices*, Phys. Rev. Lett. **123**, 046601 (2019).
- [49] T. Cea, P. A. Pantaleón, N. R. Walet, and F. Guinea, *Electrostatic interactions in twisted bilayer graphene*, Nano Materials Science **4**, 27 (2022).
- [50] One important limitation of the weak-coupling approach is that it does not capture the influence of unordered fluctuating local moments.
- [51] A more complete set of numerical results for a wide variety of filling factors and flavor polarizations are gathered in SM X Table I.
- [52] S. Liu, E. Khalaf, J. Y. Lee, and A. Vishwanath, *Nematic topological semimetal and insulator in magic-angle bilayer graphene at charge neutrality*, Phys. Rev. Res. **3**, 013033 (2021).
- [53] M. Yankowitz, S. Chen, H. Polshyn, Y. Zhang, K. Watanabe, T. Taniguchi, D. Graf, A. F. Young, and C. R. Dean, *Tuning superconductivity in twisted bilayer graphene*, Science **363**, 1059 (2019).
- [54] A. L. Sharpe, E. J. Fox, A. W. Barnard, J. Finney, K. Watanabe, T. Taniguchi, M. A. Kastner, and D. Goldhaber-Gordon, *Evidence of orbital ferromagnetism in twisted bilayer graphene aligned to hexagonal boron nitride*, Nano letters **21**, 4299 (2021).
- [55] H. C. Po, L. Zou, T. Senthil, and A. Vishwanath, *Faithful tight-binding models and fragile topology of magic-angle bilayer graphene*, Phys. Rev. B **99**, 195455 (2019).
- [56] E. Khalaf, N. Bultinck, A. Vishwanath, and M. P. Zaletel, *Soft modes in magic angle twisted bilayer graphene*, arXiv:2009.14827 (2020).
- [57] A. Kumar, M. Xie, and A. H. MacDonald, *Lattice collective modes from a continuum model of magic-angle twisted bilayer graphene*, Phys. Rev. B **104**, 035119 (2021).
- [58] Z.-D. Song and B. A. Bernevig, *Magic-angle twisted bilayer graphene as a topological heavy fermion problem*, Phys. Rev. Lett. **129**, 047601 (2022).
- [59] P. Potasz, M. Xie, and A. H. MacDonald, *Exact diagonalization for magic-angle twisted bilayer graphene*, Phys. Rev. Lett. **127**, 147203 (2021).
- [60] C. Repellin, Z. Dong, Y.-H. Zhang, and T. Senthil, *Ferromagnetism in narrow bands of moiré superlattices*, Phys. Rev. Lett. **124**, 187601 (2020).
- [61] F. Xie, A. Cowsik, Z.-D. Song, B. Lian, B. A. Bernevig, and N. Regnault, *Twisted bilayer graphene. VI. an exact diagonalization study at nonzero integer filling*, Phys. Rev. B **103**, 205416 (2021).
- [62] T. Soejima, D. E. Parker, N. Bultinck, J. Hauschild, and M. P. Zaletel, *Efficient simulation of moiré materials using the density matrix renormalization group*, Phys. Rev. B **102**, 205111 (2020).
- [63] J. P. Eisenstein, L. N. Pfeiffer, and K. W. West, *Negative compressibility of interacting two-dimensional electron and quasi-particle gases*, Phys. Rev. Lett. **68**, 674 (1992).
- [64] G. L. Yu, R. Jalil, B. Belle, A. S. Mayorov, P. Blake, F. Schedin, S. V. Morozov, L. A. Ponomarenko, F. Chiappini, S. Wiedmann, U. Zeitler, M. I. Katsnelson, A. K. Geim, K. S. Novoselov, and D. C. Elias, *Interaction phenomena in graphene seen through quantum capacitance*, Proceedings of the National Academy of Sciences **110**, 3282 (2013).
- [65] M. Brando, D. Belitz, F. M. Grosche, and T. R. Kirkpatrick, *Metallic quantum ferromagnets*, Rev. Mod. Phys. **88**, 025006 (2016).
- [66] S. Fang, S. Carr, Z. Zhu, D. Massatt, and E. Kaxiras, *Angle-dependent ab initio low-energy Hamiltonians for a relaxed twisted bilayer graphene heterostructure*, arXiv:1908.00058 (2019).
- [67] S. Carr, S. Fang, Z. Zhu, and E. Kaxiras, *Exact continuum model for low-energy electronic states of twisted bilayer graphene*, Phys. Rev. Res. **1**, 013001 (2019).
- [68] O. Vafek and J. Kang, *Continuum effective Hamiltonian for graphene bilayers for an arbitrary smooth lattice deformation from microscopic theories*, Phys. Rev. B **107**, 075123 (2023).
- [69] J. Kang and O. Vafek, *Pseudomagnetic fields, particle-hole asymmetry, and microscopic effective continuum Hamiltonians of twisted bilayer graphene*, Phys. Rev. B **107**, 075408 (2023).
- [70] G. Tarnopolsky, A. J. Kruchkov, and A. Vishwanath, *Origin of magic angles in twisted bilayer graphene*, Phys. Rev. Lett. **122**, 106405 (2019).
- [71] N. Bultinck, E. Khalaf, S. Liu, S. Chatterjee, A. Vishwanath, and M. P. Zaletel, *Ground state and hidden symmetry of magic-angle graphene at even integer filling*, Phys. Rev. X **10**, 031034 (2020).
- [72] E. Khalaf, P. Ledwith, and A. Vishwanath, *Symmetry constraints on superconductivity in twisted bilayer graphene: Fractional vortices, $4e$ condensates, or nonunitary pairing*, Phys. Rev. B **105**, 224508 (2022).
- [73] M. Kashiwagi, T. Taen, K. Uchida, K. Watanabe, T. Taniguchi, and T. Osada, *Weak localization on moiré superlattice in twisted double bilayer graphene*, Jpn. J. Appl. Phys. **61**, 100907 (2022).
- [74] J. Kang, B. A. Bernevig, and O. Vafek, *Cascades between light and heavy fermions in the normal state of magic-angle twisted bilayer graphene*, Phys. Rev. Lett. **127**, 266402 (2021).
- [75] R. Geick, C. H. Perry, and G. Rupprecht, *Normal modes in hexagonal boron nitride*, Phys. Rev. **146**, 543 (1966).

- [76] G. Giuliani and G. Vignale, *Quantum Theory of the Electron Liquid* (2005).
- [77] A. Görling, *Hierarchies of methods towards the exact kohnsham correlation energy based on the adiabatic-connection fluctuation-dissipation theorem*, Phys. Rev. B **99**, 235120 (2019).
- [78] Y. H. Kwan, G. Wagner, T. Soejima, M. P. Zaletel, S. H. Simon, S. A. Parameswaran, and N. Bultinck, *Kekulé spiral order at all nonzero integer fillings in twisted bilayer graphene*, Phys. Rev. X **11**, 041063 (2021).
- [79] P. J. Ledwith, E. Khalaf, and A. Vishwanath, *Strong coupling theory of magic-angle graphene: A pedagogical introduction*, Annals of Physics **435**, 168646 (2021).
- [80] G. Shavit, E. Berg, A. Stern, and Y. Oreg, *Theory of correlated insulators and superconductivity in twisted bilayer graphene*, Phys. Rev. Lett. **127**, 247703 (2021).
- [81] G. Shavit, K. c. v. Kolář, C. Mora, F. von Oppen, and Y. Oreg, *Strain disorder and gapless intervalley coherent phase in twisted bilayer graphene*, Phys. Rev. B **107**, L081403 (2023).
- [82] M. Oh, K. P. Nuckolls, D. Wong, R. L. Lee, X. Liu, K. Watanabe, T. Taniguchi, and A. Yazdani, *Evidence for unconventional superconductivity in twisted bilayer graphene*, Nature **600**, 240 (2021).
- [83] J. P. Hong, T. Soejima, and M. P. Zaletel, *Detecting symmetry breaking in magic angle graphene using scanning tunneling microscopy*, Phys. Rev. Lett. **129**, 147001 (2022).
- [84] J. Yu, B. A. Foutty, Y. H. Kwan, M. E. Barber, K. Watanabe, T. Taniguchi, Z.-X. Shen, S. A. Parameswaran, and B. E. Feldman, *Spin skyrmion gaps as signatures of intervalley-coherent insulators in magic-angle twisted bilayer graphene*, Nature Communications **14**, 6679 (2023).
- [85] K. P. Nuckolls, R. L. Lee, M. Oh, D. Wong, T. Soejima, J. P. Hong, D. Călugăru, J. Herzog-Arbeitman, B. A. Bernevig, K. Watanabe, T. Taniguchi, N. Regnault, M. P. Zaletel, and A. Yazdani, *Quantum textures of the many-body wavefunctions in magic-angle graphene*, Nature **620**, 525 (2023).
- [86] See e.g. Ref.[77] and references therein to earlier work.

Supplemental Material: Weak Coupling Theory of Competing Phases in Magic-Angle Twisted Bilayer Graphene

I. BISTRITZER-MACDONALD MODEL WITH NON-LOCAL INTERLAYER TUNNELING

In the original Bistritzer-MacDonald (BM) model, Eq. (5) in Ref. [1], the interlayer tunneling matrix element is

$$\begin{aligned} T_{\mathbf{k}\mathbf{k}'}^{\alpha\beta} &= \frac{1}{A_{uc}} \sum_{j=1}^3 t_{\mathbf{k}+\mathbf{G}_j} e^{i[\mathbf{G}_j \cdot (\tau_\alpha - \tau_\beta + \tau_0) - \mathbf{G}'_j \cdot \mathbf{d}]} \delta_{\mathbf{k}+\mathbf{G}_j, \mathbf{k}'+\mathbf{G}'_j} \\ &= \frac{1}{A_{uc}} \sum_{j=1}^3 t_{\mathbf{k}+\mathbf{G}_j} T_j^{\alpha\beta} \delta_{\mathbf{k}+\mathbf{G}_j, \mathbf{k}'+\mathbf{G}'_j}, \end{aligned} \quad (7)$$

where \mathbf{G} and \mathbf{G}' are reciprocal lattice vectors of the top (layer 1) and bottom (layer 2) graphene layers respectively, momenta \mathbf{k} and \mathbf{k}' are measured relative to the Γ point of the original monolayer graphene and are both near the Dirac point \mathbf{K} . Greek indices label sublattices. The interlayer tunneling t and matrices T_j are defined later. The top layer (layer 1) is anticlockwise rotated by $\theta/2$ and characterized by vectors without $'$ in the notation, bottom layer (layer 2) is clockwise rotated by $\theta/2$ and characterized by vector with $'$. The reciprocal lattice vectors are related by the rotation operator $\mathbf{G}'_i = \mathcal{R}_{-\theta} \mathbf{G}_i$, with

$$\mathcal{R}_\theta = \begin{pmatrix} \cos \theta & -\sin \theta \\ \sin \theta & \cos \theta \end{pmatrix}. \quad (8)$$

Three \mathbf{G} 's that are most relevant to the interlayer hopping in the two-center approximation are, as shown in Fig. 4(a),

$$\mathbf{G}_1 = \begin{pmatrix} 0 \\ 0 \end{pmatrix}, \quad \mathbf{G}_2 = \mathcal{R}_{\theta/2} \cdot \frac{4\pi}{\sqrt{3}a} \begin{pmatrix} -\frac{\sqrt{3}}{2} \\ \frac{1}{2} \end{pmatrix}, \quad \mathbf{G}_3 = \mathcal{R}_{\theta/2} \cdot \frac{4\pi}{\sqrt{3}a} \begin{pmatrix} -\frac{\sqrt{3}}{2} \\ -\frac{1}{2} \end{pmatrix}. \quad (9)$$

$a = 0.246$ nm is graphene's lattice constant. Starting from AB-stacked bilayer graphene, we choose

$$\tau_A = \begin{pmatrix} 0 \\ 0 \end{pmatrix}, \quad \tau_B = \tau_0 = \mathcal{R}_{\theta/2} \cdot \frac{a}{\sqrt{3}} \begin{pmatrix} 0 \\ 1 \end{pmatrix}. \quad (10)$$

Three largest interlayer hopping terms, corresponding to three \mathbf{G} 's in Eq. (9), are

$$T_1 = \begin{pmatrix} u & 1 \\ 1 & u \end{pmatrix}, \quad T_2 = e^{-i\mathbf{G}'_2 \cdot \mathbf{d}} \begin{pmatrix} ue^{i\phi} & 1 \\ e^{-i\phi} & ue^{i\phi} \end{pmatrix}, \quad T_3 = e^{-i\mathbf{G}'_3 \cdot \mathbf{d}} \begin{pmatrix} ue^{-i\phi} & 1 \\ e^{i\phi} & ue^{-i\phi} \end{pmatrix}, \quad (11)$$

where $\phi = 2\pi/3$, $u = w_{AA}/w_{AB}$ is the ratio of interlayer tunneling between the same sublattice and between different sublattices. The phase factor dependent on \mathbf{d} can be eliminated by a unitary transformation of the plane-wave expanded basis.

The Fourier transform of interlayer tunneling strength $t(\mathbf{r})$ in Eq. (7) is

$$t_{\mathbf{q}} = \int d^2\mathbf{r} e^{i\mathbf{q} \cdot \mathbf{r}} t(\mathbf{r}). \quad (12)$$

Because $t(\mathbf{r})$ is a smooth and slowly varying function of the projected 2D coordinate \mathbf{r} , $t_{\mathbf{q}}$ rapidly decays with respect to q and we only keep three terms in the interlayer tunneling Eq. (7). Because of the symmetry of carbon p_z orbitals, $t(\mathbf{r})$ and therefore $t_{\mathbf{q}}$ are orientation-independent, i.e. $t_{\mathbf{q}} = t_q$.

As shown in Fig. 4(b), the three allowed momentum boosts, defined by the difference between the momenta in the top and bottom layers $\tilde{\mathbf{g}}_j = \mathbf{k} - \mathbf{k}' = \mathbf{G}'_j - \mathbf{G}_j$, are

$$\tilde{\mathbf{g}}_1 = \begin{pmatrix} 0 \\ 0 \end{pmatrix}, \quad \tilde{\mathbf{g}}_2 = \frac{4\pi}{\sqrt{3}a_M} \begin{pmatrix} \frac{1}{2} \\ \frac{\sqrt{3}}{2} \end{pmatrix}, \quad \tilde{\mathbf{g}}_3 = \frac{4\pi}{\sqrt{3}a_M} \begin{pmatrix} -\frac{1}{2} \\ \frac{\sqrt{3}}{2} \end{pmatrix}, \quad (13)$$

where $a_M = a/(2 \sin(\theta/2)) \approx a/\theta$ is the moiré lattice constant.

Momenta $\mathbf{k} + \mathbf{G}_j$ in Eq. (7) are near Brillouin zone corners. To zeroth order,

$$t_{\mathbf{k}+\mathbf{G}_j} \approx t_{\mathbf{k}_{D,j}} = t_{k_D} = w_0 A_{uc}, \quad (14)$$

where $\mathbf{k}_{D,j}$ are Dirac points of the unrotated graphene

$$\mathbf{k}_{D,j} = e^{i2\pi(j-1)/3} (1, 0) \frac{4\pi}{3a}. \quad (15)$$

The interlayer tunneling is local and therefore momentum independent

$$T_{\mathbf{k}\mathbf{k}'} = w_0 \sum_{j=1}^3 T_j \delta_{\mathbf{k}-\mathbf{k}', \tilde{\mathbf{g}}_j}. \quad (16)$$

The approximate particle-hole symmetry is broken by taking into account non-local interlayer tunneling effects[47]. Keeping the expansion in $t_{\mathbf{k}+\mathbf{G}_j}$ till the first order,

$$t_{\mathbf{k}} \approx t_{k_D} + t'(k - k_D), \quad (17)$$

where

$$t' = \left. \frac{dt}{dk} \right|_{k=k_D} < 0 \quad (18)$$

is the tunable non-local tunneling parameter. The momentum-dependent interlayer tunneling becomes

$$\begin{aligned} T_{\mathbf{k}\mathbf{k}'} &= \frac{1}{A_{uc}} \sum_{j=1}^3 t_{\mathbf{k}+\mathbf{G}_j} T_j \delta_{\mathbf{k}-\mathbf{k}', \tilde{\mathbf{g}}_j} \\ &= \sum_{j=1}^3 \left[w_0 + \frac{w_{nl}}{g_M} (|\mathbf{k} + \mathbf{G}_j| - k_D) \right] T_j \delta_{\mathbf{k}-\mathbf{k}', \tilde{\mathbf{g}}_j}. \end{aligned} \quad (19)$$

The non-local tunneling parameter w_{nl} is defined as

$$w_{nl} = \frac{g_M}{A_{uc}} t', \quad (20)$$

where $g_M = 4\pi/\sqrt{3}a_M$ is the length of moiré primitive reciprocal lattice vector.

In the numerical calculations in this Letter, we take $v_F = 0.866 \times 10^6$ m/s, $u = w_{AA}/w_{AB} = 0.6$, $w_0 = 110$ meV and $w_{nl} = -20$ meV for MATBG of twist angle 1.1° . For other efforts to improve the accuracy of the single-particle Hamiltonian of twisted bilayer graphene see Refs. [66–69].

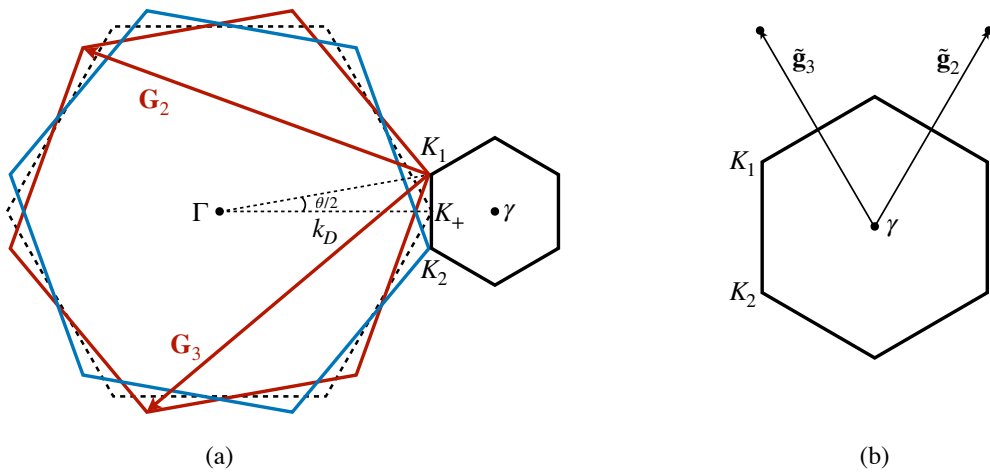


FIG. 4. (a) Rotated Brillouin zones of top (red) and bottom (blue) graphene layers. The top layer is rotated anticlockwise with respect to the bottom layer by θ . The black dashed hexagonal is the Brillouin zone of unrotated graphene. K_+ , K_1 and K_2 are Dirac points of unrotated graphene, the top graphene layer and the bottom graphene layer respectively. k_D is the length of $\Gamma - K_+$. The smaller black hexagon on the right is the moiré Brillouin zone. (b) The moiré Brillouin zone. Three momentum boosts $\tilde{\mathbf{g}}_j$ in Eq. (13) are shown.

II. TBG HAMILTONIAN

The Hamiltonian of a periodic crystal is

$$\hat{H} = \hat{T}_e + \hat{H}_{e-e} + \hat{H}_{e-b} + \hat{H}_{b-b}, \quad (21)$$

where \hat{T}_e is the kinetic energy operator. Instead of the uniform background charge in the Jellium model, a periodic background of the positive charge

$$n_b(\mathbf{r}) = \frac{1}{A} \sum_{\mathbf{G}} n_{b,\mathbf{G}} e^{i\mathbf{G}\cdot\mathbf{r}} \quad (22)$$

is assumed. At CN, the background charge cancels with excess electron charge

$$n_{b,0} = \int n_b(\mathbf{r}) d\mathbf{r} = N. \quad (23)$$

Written in electron number density operators $\hat{n}(\mathbf{q})$ and the total number operator \hat{N}

$$\begin{aligned} \hat{n}(\mathbf{q}) &= \sum_{\mathbf{k}, \mathbf{G}} c_{\mathbf{k}+\mathbf{G}-\mathbf{q}}^\dagger c_{\mathbf{k}+\mathbf{G}}, \\ \hat{N} = \hat{n}(\mathbf{q}=0) &= \sum_{\mathbf{k}, \mathbf{G}} c_{\mathbf{k}+\mathbf{G}}^\dagger c_{\mathbf{k}+\mathbf{G}}, \end{aligned} \quad (24)$$

the interacting Hamiltonians are

$$\begin{aligned} \hat{H}_{e-b} &= -e^2 \int d\mathbf{r} d\mathbf{r}' \frac{\hat{n}(\mathbf{r}) n_b(\mathbf{r}')}{|\mathbf{r} - \mathbf{r}'|} = -\frac{1}{A} \sum_{\mathbf{G}} V(\mathbf{G}) n_{b,\mathbf{G}} \hat{n}_{-\mathbf{G}}, \\ \hat{H}_{b-b} &= \frac{e^2}{2} \int d\mathbf{r} d\mathbf{r}' \frac{n_b(\mathbf{r}) n_b(\mathbf{r}')}{|\mathbf{r} - \mathbf{r}'|} = \frac{1}{2A} \sum_{\mathbf{G}} V(\mathbf{G}) n_{b,\mathbf{G}} n_{b,-\mathbf{G}}, \\ \hat{H}_{e-e} &= \frac{e^2}{2} \sum_{i \neq j} \frac{1}{|\mathbf{r}_i - \mathbf{r}_j|} = \frac{1}{2A} \sum_{\mathbf{q}, \mathbf{G}} V(\mathbf{q} + \mathbf{G}) [\hat{n}(\mathbf{q} + \mathbf{G}) \hat{n}(-\mathbf{q} - \mathbf{G}) - \hat{N}]. \end{aligned} \quad (25)$$

Similar to the Jellium model, the $\mathbf{G} = 0$ terms of \hat{H}_{e-b} and \hat{H}_{b-b} , and the $\mathbf{q} = \mathbf{G} = 0$ term of \hat{H}_{e-e} cancel in the thermodynamic limit $A, N \rightarrow \infty$. The full Hamiltonian in Eq. (21) can be written as

$$\begin{aligned} \hat{H} &= \hat{T}_e + \hat{H}_{e-e} + \hat{V}_b \\ &= \hat{T}_e + \frac{1}{2A} \sum'_{\mathbf{q}, \mathbf{G}} V(\mathbf{q} + \mathbf{G}) [\hat{n}(\mathbf{q} + \mathbf{G}) \hat{n}(-\mathbf{q} - \mathbf{G}) - \hat{N}] + \frac{1}{2A} \sum_{\mathbf{G} \neq 0} V(\mathbf{G}) [-2n_{b,\mathbf{G}} \hat{n}_{-\mathbf{G}} + n_{b,\mathbf{G}} n_{b,-\mathbf{G}}], \end{aligned} \quad (26)$$

where ' on the summation symbol means $\mathbf{q} = \mathbf{G} = 0$ term is excluded in the momentum summation.

It is straightforward to generalize the electron-electron interacting Hamiltonian in Eq. (26) to the TBG case, where two layers and two sublattices degrees of freedom are explicitly included,

$$\hat{H}_{e-e} = \frac{1}{2A} \sum'_{\substack{\mathbf{q}, \mathbf{g}, \alpha, \beta \\ \mathbf{k}_1, \mathbf{k}_2, \mathbf{g}_1, \mathbf{g}_2}} V_{\alpha\beta}(\mathbf{q} + \mathbf{g}) c_{\alpha, \mathbf{k}_1 + \mathbf{g}_1 - \mathbf{q} - \mathbf{g}}^\dagger c_{\beta, \mathbf{k}_2 + \mathbf{g}_2 + \mathbf{q} + \mathbf{g}}^\dagger c_{\beta, \mathbf{k}_2 + \mathbf{g}_2} c_{\alpha, \mathbf{k}_1 + \mathbf{g}_1}, \quad (27)$$

where $\mathbf{g}, \mathbf{g}_1, \mathbf{g}_2$ are moiré reciprocal lattice vectors and $\mathbf{k}_1, \mathbf{k}_2, \mathbf{q}$ are momenta in the first moiré Brillouin zone. α, β label layers and sublattices. The ' on top of the summation means the $\mathbf{q} = \mathbf{g} = 0$ term is excluded, which is cancelled by the periodic background of positive charge in the thermodynamic limit.

Alternatively, \hat{H}_{e-e} can be expressed in electron number density operators

$$\hat{H}_{e-e} = -\frac{1}{2A} \sum'_{\mathbf{q}, \mathbf{g}} V_S(\mathbf{q} + \mathbf{g}) \hat{N} + \frac{1}{2A} \sum'_{\substack{\mathbf{q}, \mathbf{g} \\ \alpha, \beta}} V_{\alpha\beta}(\mathbf{q} + \mathbf{g}) \sum_{\mathbf{g}_1, \mathbf{g}_2} \hat{n}_{\alpha}^{\mathbf{g}_1}(\mathbf{q} + \mathbf{g}) \hat{n}_{\beta}^{\mathbf{g}_2}(-\mathbf{q} - \mathbf{g}), \quad (28)$$

where

$$\begin{aligned}\hat{N} &= \sum_{\mathbf{k}, \mathbf{g}, \alpha} c_{\alpha, \mathbf{k}+\mathbf{g}}^\dagger c_{\alpha, \mathbf{k}+\mathbf{g}}, \\ \hat{n}(\mathbf{q}) &= \sum_{\alpha, \mathbf{g}} \hat{n}_{\alpha}^{\mathbf{g}}(\mathbf{q}) = \sum_{\alpha, \mathbf{g}} \sum_{\mathbf{k}} c_{\alpha, \mathbf{k}+\mathbf{g}-\mathbf{q}}^\dagger c_{\alpha, \mathbf{k}+\mathbf{g}}.\end{aligned}\quad (29)$$

For isotropic dielectric media, the Coulomb interaction within the same 2D layer (V_S) and between different 2D layers (V_D) are respectively

$$\begin{aligned}V_S(\mathbf{q}) &= \frac{2\pi e^2}{\epsilon q}, \\ V_D(\mathbf{q}) &= \frac{2\pi e^2}{\epsilon q} e^{-qd},\end{aligned}\quad (30)$$

where ϵ is the relative dielectric constant of the surrounding environment and d is the distance between adjacent layers.

For anisotropic dielectric media, for example hBN, $\epsilon_{\text{BN}} = \sqrt{\epsilon_{zz}\epsilon_{\perp}} \approx 4.5$ with $\epsilon_{\perp} = 6.9$ [75], $\epsilon_{zz} = 3$.

$$\begin{aligned}V_S(\mathbf{q}) &= \frac{2\pi e^2}{q\sqrt{\epsilon_{\perp}\epsilon_{zz}}}, \\ V_D(\mathbf{q}) &= \frac{2\pi e^2}{q\sqrt{\epsilon_{\perp}\epsilon_{zz}}} e^{-qd\sqrt{\epsilon_{\perp}/\epsilon_{zz}}}.\end{aligned}\quad (31)$$

With dual metallic gates that is equidistant from the target 2D system, with distance d_m , the screened Coulomb potential energy is

$$V_{sc}(\mathbf{q}) = \frac{2\pi e^2}{q\sqrt{\epsilon_{\perp}\epsilon_{zz}}} \tanh\left(qd_m\sqrt{\frac{\epsilon_{\perp}}{\epsilon_{zz}}}\right).\quad (32)$$

In calculations throughout this paper, the d -dependence of the Coulomb potential in Eq. (31) is ignored, *i.e.*,

$$V(\mathbf{q}) = V_S(\mathbf{q}) = V_D(\mathbf{q}) = \frac{2\pi e^2}{q\epsilon_{\text{BN}}},\quad (33)$$

and the hBN dielectric constant is chosen to be $\epsilon_{\text{BN}} = 5.1$. Then Eq. (28) simplifies to

$$\hat{H}_{e-e} = \frac{1}{2A} \sum_{\mathbf{q}, \mathbf{g}} V(\mathbf{q} + \mathbf{g}) \left[\hat{n}(\mathbf{q} + \mathbf{g}) \hat{n}(-\mathbf{q} - \mathbf{g}) - \hat{N} \right].\quad (34)$$

III. SELF-CONSISTENT HARTREE APPROXIMATION IN TBG

With approximate SU(4) symmetry, the exchange interaction is only between electrons within the same flavor. The inter-flavor interaction is only through the Hartree potential. The matrix element of the flavor- and momentum-independent Hartree self-energy is

$$\Sigma_{\alpha, \mathbf{g}_1; \beta, \mathbf{g}_2}^H = \frac{\delta_{\alpha\beta}}{A} \sum_{\alpha', \mathbf{g}'_1, \mathbf{g}'_2} V_{\alpha\alpha'}(\mathbf{g}_2 - \mathbf{g}_1) \delta\rho_{\alpha'; \mathbf{g}'_1; \alpha', \mathbf{g}'_2} \delta_{\mathbf{g}'_2 - \mathbf{g}'_1, \mathbf{g}_2 - \mathbf{g}_1},\quad (35)$$

where $\delta\rho$ is the relative density matrix defined by subtracting the density matrix of the decoupled graphene bilayer at CN

$$\delta\rho = \rho - \rho_0.\quad (36)$$

The flavor-polarization-dependence of the self-energy is implicitly incorporated in the density matrix through the Fermi-Dirac distribution $\Theta(\mu_f - \epsilon_{nk}^f)$:

$$\rho_{\alpha, \mathbf{g}_1; \beta, \mathbf{g}_2} = \sum_{f, n, \mathbf{k}} z_{\alpha, \mathbf{g}_1}^{nf}(\mathbf{k}) z_{\beta, \mathbf{g}_2}^{nf}(\mathbf{k}) \Theta(\mu_f - \epsilon_{nk}^f).\quad (37)$$

$f = 1, 2, 3, 4$ represent four flavors. If the inversion symmetry is retained, the diagonal elements of Σ^H are constant and can be set to zero.

For any specific flavor polarization $(\nu_1, \nu_2, \nu_3, \nu_4)$, the Hamiltonian is solved self-consistently for each flavor

$$H^f(\mathbf{k}, \nu_1, \nu_2, \nu_3, \nu_4) = H_0^f(\mathbf{k}) + \Sigma^H(\nu_1, \nu_2, \nu_3, \nu_4), \quad (38)$$

where $H_0^f(\mathbf{k})$ is the single-particle Hamiltonian of flavor f .

Self-consistent Hartree band structures and corresponding Fermi surfaces of flavor-symmetry unbroken states at filling factors $\nu \in (-1, 1)$ are shown in Fig. 5.

The electrostatic Hartree energy is

$$\begin{aligned} E_H &= \frac{1}{2} \sum_{f,n,\mathbf{k}} \langle \Psi_{fn\mathbf{k}} | \Sigma^H | \Psi_{fn\mathbf{k}} \rangle \Theta(\mu_f - \varepsilon_{n\mathbf{k}}^f) \\ &= \frac{1}{2A} \sum_{\substack{\mathbf{g}_1, \mathbf{g}_2 \\ \mathbf{g}'_1, \mathbf{g}'_2}} \sum_{\alpha, \alpha'} V_{\alpha\alpha'}(\mathbf{g}_2 - \mathbf{g}_1) \bar{\rho}_{\alpha, \mathbf{g}_1; \alpha, \mathbf{g}_2} \delta \rho_{\alpha', \mathbf{g}'_1; \alpha', \mathbf{g}'_2} \delta_{\mathbf{g}'_2 - \mathbf{g}'_1, \mathbf{g}_2 - \mathbf{g}_1}, \end{aligned} \quad (39)$$

and is further regularized by subtracting the negative Fermi sea contribution

$$E_H = \frac{1}{2A} \sum_{\substack{\mathbf{g}_1, \mathbf{g}_2 \\ \mathbf{g}'_1, \mathbf{g}'_2}} \sum_{\alpha, \alpha'} V_{\alpha\alpha'}(\mathbf{g}_2 - \mathbf{g}_1) \delta \bar{\rho}_{\alpha, \mathbf{g}_1; \alpha, \mathbf{g}_2} \delta \rho_{\alpha', \mathbf{g}'_1; \alpha', \mathbf{g}'_2} \delta_{\mathbf{g}'_2 - \mathbf{g}'_1, \mathbf{g}_2 - \mathbf{g}_1}. \quad (40)$$

The SCH energy E_0 in the main text is defined to include both the SCH band dispersion and the electrostatic Hartree energy:

$$\begin{aligned} E_0 &= E_{\text{band}} - E_H \\ &= \sum_{f,n,\mathbf{k}} \varepsilon_{n\mathbf{k}}^f \Theta(\mu_f - \varepsilon_{n\mathbf{k}}^f) - E_H, \end{aligned} \quad (41)$$

where $\varepsilon_{n\mathbf{k}}^f$ are eigenvalues of SCH Hamiltonian Eq. (38) and E_H is subtracted to avoid double-counting of the Coulomb energy.

IV. SELF-CONSISTENT HARTREE-FOCK FERMI SURFACES

To compare with the self-consistent Hartree approximation, we present in Fig. 6 the Fermi surfaces of self-consistent Hartree-Fock calculations with momentum- and flavor-dependent Fock self-energy

$$\Sigma_{\alpha, \mathbf{g}_1; \beta, \mathbf{g}_2}^{F,f}(\mathbf{k}) = -\frac{1}{A} \sum_{\mathbf{k}', \mathbf{g}'_1, \mathbf{g}'_2} V_{\alpha\beta}(\mathbf{k}' - \mathbf{k} + \mathbf{g}'_1 - \mathbf{g}_1) \delta \rho_{\alpha, \mathbf{g}'_1; \beta, \mathbf{g}'_2}^f(\mathbf{k}') \delta_{\mathbf{g}'_2 - \mathbf{g}'_1, \mathbf{g}_2 - \mathbf{g}_1}. \quad (42)$$

V. THE DENSITY RESPONSE FUNCTION OF TBG

At zero temperature, the matrix elements of the flavor-specified density response function $\tilde{\chi}^f$ of MATBG can be derived following the Lindhard formula

$$[\tilde{\chi}^f]^{\mathbf{g}\mathbf{g}'}(\mathbf{q}, \omega) = \frac{1}{A} \sum_{n,m,\mathbf{k}} \frac{\Theta_{n\mathbf{k}}^f - \Theta_{m\mathbf{k}+\mathbf{q}}^f}{\omega + \varepsilon_{n\mathbf{k}}^f - \varepsilon_{m\mathbf{k}+\mathbf{q}}^f + i\eta} \left[\sum_{\alpha, \mathbf{g}_1} z_{\alpha, \mathbf{g}_1}^{nf}(\mathbf{k}) z_{\alpha, \mathbf{g}_1 + \mathbf{g}}^{mf}(\mathbf{k} + \mathbf{q}) \right]^* \sum_{\beta, \mathbf{g}_2} z_{\beta, \mathbf{g}_2}^{nf}(\mathbf{k}) z_{\beta, \mathbf{g}_2 + \mathbf{g}'}^{mf}(\mathbf{k} + \mathbf{q}). \quad (43)$$

where ε and z are quasiparticle eigen-energy and eigenvector of the self-consistent Hartree approximation. It can be easily proved that Eq. (43) satisfies the symmetry

$$[\tilde{\chi}^f]^{\mathbf{g}\mathbf{g}'}(\mathbf{q}, \omega) = [[\tilde{\chi}^f]^{-\mathbf{g}-\mathbf{g}'}(-\mathbf{q}, -\omega)]^*. \quad (44)$$

It obeys the general property of the response function

$$\tilde{\chi}_{AB}(\omega) = [\tilde{\chi}_{A^\dagger B^\dagger}(-\omega)]^*. \quad (45)$$

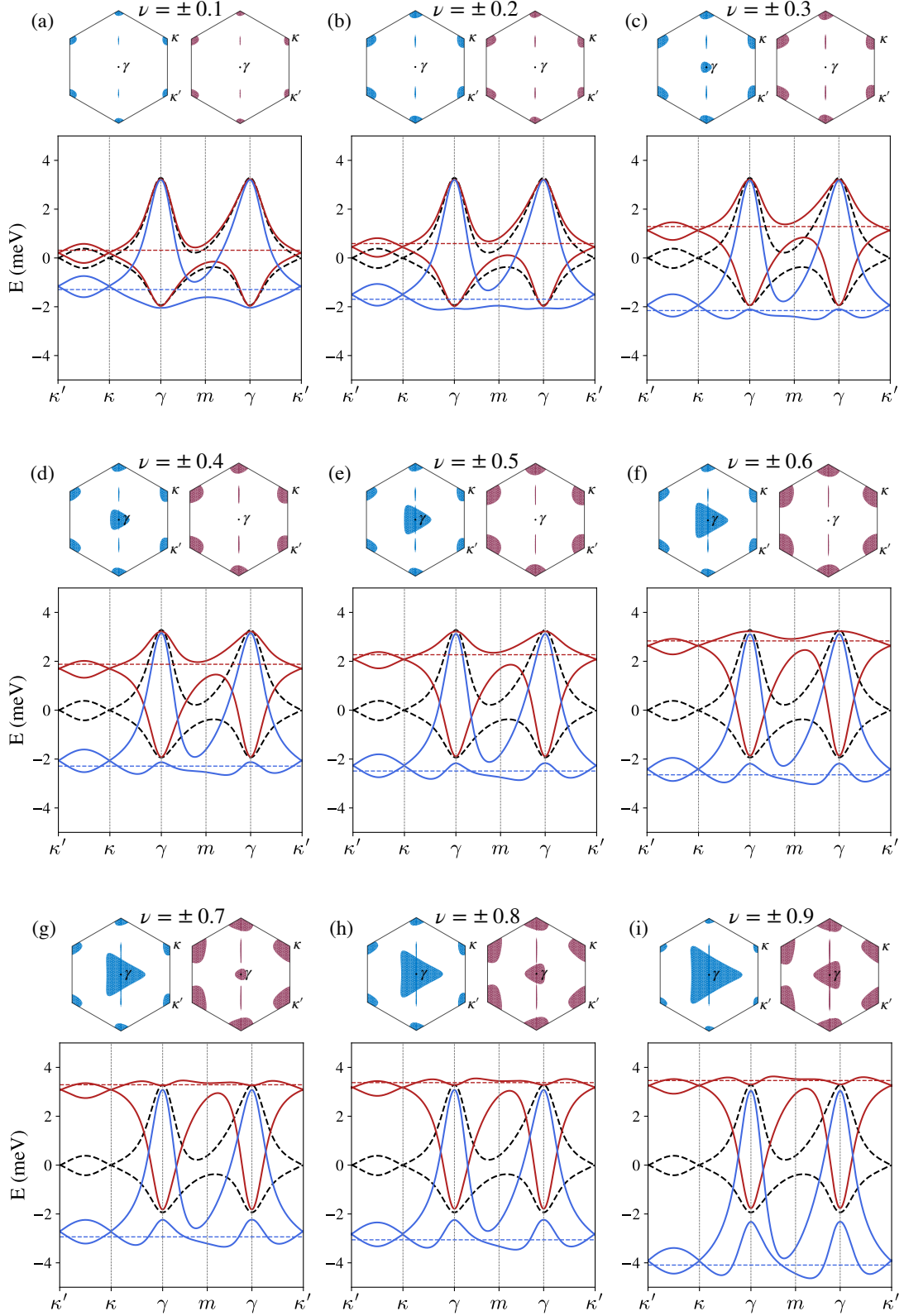


FIG. 5. Self-consistent Hartree band structures (colored lines) and corresponding Fermi surfaces (colored shaded areas) of flavor paramagnetic states at filling factors $\nu \in (-1, 1)$. Red (blue) represents electron (hole) doping. The black dashed line in each spectrum is the single-particle band structure. Note that the energy bands and the Fermi levels are shifted such that the non-interacting band energy at κ is zero.

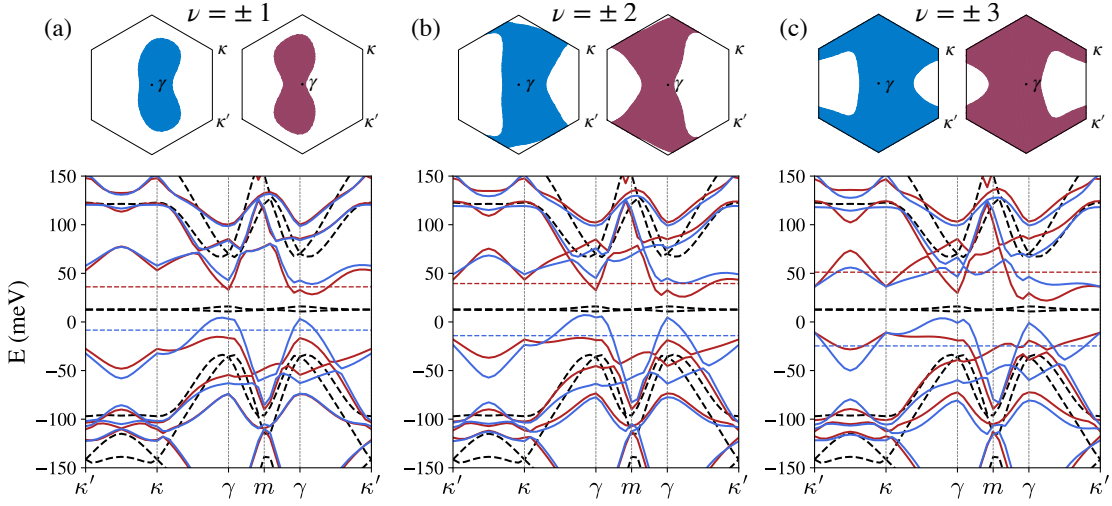


FIG. 6. Self-consistent Hartree-Fock band structures (colored lines) and corresponding Fermi surfaces (colored shaded areas) of flavor paramagnetic states at filling factors $\nu = \pm 1, \pm 2, \pm 3$. Red (blue) represents electron (hole) doping. The black dashed line in each spectrum is the single-particle band structure.

The density response functions of opposite valleys with the same electrostatic doping level are related by the spinless time-reversal symmetry

$$[\tilde{\chi}^-]^{\mathbf{g}\mathbf{g}'}(\mathbf{q}, \omega) = [\tilde{\chi}^+]^{-\mathbf{g}'-\mathbf{g}}(-\mathbf{q}, \omega), \quad (46)$$

following reciprocity relations

$$\tilde{\chi}_{AB}^-(\omega) = \tilde{\chi}_{B^T A^T}^+(\omega), \quad (47)$$

where \pm represent two opposite valleys in TBG. If the TBG system is flavor unpolarized, the total density response function $\tilde{\chi}$ summed over four flavors is time-reversal invariant and satisfies

$$\begin{aligned} \tilde{\chi}^{\mathbf{g}\mathbf{g}'}(\mathbf{q}, \omega) &= 2[\tilde{\chi}^+]^{\mathbf{g}\mathbf{g}'}(\mathbf{q}, \omega) + 2[\tilde{\chi}^-]^{\mathbf{g}\mathbf{g}'}(\mathbf{q}, \omega) \\ &= 2[\tilde{\chi}^+]^{\mathbf{g}\mathbf{g}'}(\mathbf{q}, \omega) + 2[\tilde{\chi}^+]^{-\mathbf{g}'-\mathbf{g}}(-\mathbf{q}, \omega) \\ &= \tilde{\chi}^{-\mathbf{g}'-\mathbf{g}}(-\mathbf{q}, \omega). \end{aligned} \quad (48)$$

At finite temperatures, the density response function is

$$[\tilde{\chi}^f]^{\mathbf{g}\mathbf{g}'}(\mathbf{q}, i\omega) = \frac{1}{A} \sum_{n,m,\mathbf{k}} \frac{\Theta_{n\mathbf{k}}^f - \Theta_{m\mathbf{k}+\mathbf{q}}^f}{i\omega + \varepsilon_{n\mathbf{k}}^f - \varepsilon_{m\mathbf{k}+\mathbf{q}}^f} \left[\sum_{\alpha, \mathbf{g}_1} z_{\alpha, \mathbf{g}_1}^{nf}(\mathbf{k}) z_{\alpha, \mathbf{g}_1 + \mathbf{g}}^{mf}(\mathbf{k} + \mathbf{q}) \right]^* \sum_{\beta, \mathbf{g}_2} z_{\beta, \mathbf{g}_2}^{nf}(\mathbf{k}) z_{\beta, \mathbf{g}_2 + \mathbf{g}'}^{mf}(\mathbf{k} + \mathbf{q}). \quad (49)$$

Matrix $\tilde{\chi}^f(\mathbf{q}, i\omega)$ is Hermitian along the imaginary frequency axis, *i.e.*,

$$\begin{aligned} \tilde{\chi}^f(\mathbf{q}, i\omega) &= [\tilde{\chi}^f]^\dagger(\mathbf{q}, -i\omega), \\ [\tilde{\chi}^f]^{\mathbf{g}\mathbf{g}'}(\mathbf{q}, i\omega) &= [[\tilde{\chi}^f]^{\mathbf{g}'\mathbf{g}}(\mathbf{q}, -i\omega)]^*. \end{aligned} \quad (50)$$

$\tilde{\chi}^f(\mathbf{q}, i\omega)$ also satisfies

$$[\tilde{\chi}^f]^{\mathbf{g}\mathbf{g}'}(\mathbf{q}, i\omega) = [\tilde{\chi}^f]^{-\mathbf{g}'-\mathbf{g}}(-\mathbf{q}, -i\omega) = [[\tilde{\chi}^f]^{-\mathbf{g}-\mathbf{g}'}(-\mathbf{q}, i\omega)]^*. \quad (51)$$

Opposite valleys with the same electrostatic doping level are related by the time-reversal symmetry

$$[\tilde{\chi}^-]^{\mathbf{g}\mathbf{g}'}(\mathbf{q}, i\omega) = [\tilde{\chi}^+]^{-\mathbf{g}'-\mathbf{g}}(-\mathbf{q}, i\omega) = [[\tilde{\chi}^+]^{\mathbf{g}'\mathbf{g}}(\mathbf{q}, i\omega)]^* = [[\tilde{\chi}^-]^{\mathbf{g}'\mathbf{g}}(\mathbf{q}, -i\omega)]^*. \quad (52)$$

For valley unpolarized state, the total proper density response function in Eq. (3) satisfies

$$\tilde{\chi}^{\mathbf{g}\mathbf{g}'}(\mathbf{q}, i\omega) = 2[\tilde{\chi}^+]^{\mathbf{g}\mathbf{g}'}(\mathbf{q}, i\omega) + 2[\tilde{\chi}^-]^{\mathbf{g}\mathbf{g}'}(\mathbf{q}, i\omega) = 2[\tilde{\chi}^+]^{\mathbf{g}\mathbf{g}'}(\mathbf{q}, i\omega) + 2[[\tilde{\chi}^+]^{\mathbf{g}'\mathbf{g}}(\mathbf{q}, i\omega)]^*, \quad (53)$$

and therefore the density response function of flavor unpolarized state is Hermitian, *i.e.*,

$$\tilde{\chi}(\mathbf{q}, i\omega) = \tilde{\chi}^\dagger(\mathbf{q}, i\omega). \quad (54)$$

We see that symmetries of $\tilde{\chi}(\mathbf{q}, i\omega)$ are different from those of $\tilde{\chi}(\mathbf{q}, \omega)$ at zero temperature.

VI. THE COUPLING-CONSTANT INTEGRATION AS AN EVALUATION OF THE GROUND STATE ENERGY

The ground-state energy of an electron system can be easily connected to the density-density linear-response function—for example at the level of the popular RPA — by the integration over the coupling constant theorem (see, for example, Sect. I.8.3 of Ref. [76]). However, the ground-state electron density of a moiré crystal is inhomogeneous on the moiré superlattice length scale. The application of the integration over the coupling constant theorem to an inhomogeneous many-body system is not straightforward and presents some subtleties. On the contrary, the Hohenberg-Kohn and Kohn-Sham theorems (see, for example, Chapter 7 of Ref. [76]) of density functional theory are the natural theoretical framework to deal with inhomogeneous many-body electron systems. This is why we formulate the problem of the calculation of the ground-state energy of twisted bilayer graphene within the framework of Adiabatic Connection Fluctuation and Dissipation Theorem (ACFDT) [86] and then recover the RPA by taking a suitable limit. This theory applies the integration over the coupling constant theorem between the Kohn-Sham (KS) ground state and the real ground state of the electronic Hamiltonian as detailed in the following.

A. The Adiabatic Connection Fluctuation and Dissipation Theorem

The electronic Hamiltonian can be written as

$$\hat{\mathcal{H}} = \hat{T}_e + \hat{\mathcal{H}}_{e-e} + \hat{V}_{\text{ext}} , \quad (55)$$

where \hat{T}_e is the kinetic operator, $\hat{\mathcal{H}}_{e-e}$ is the electron-electron interaction, i.e.

$$\hat{H}_{e-e} = \frac{1}{2A} \sum_{\mathbf{q}, \mathbf{G}} V(\mathbf{q} + \mathbf{G}) \left[\hat{n}(\mathbf{q} + \mathbf{G}) \hat{n}(-\mathbf{q} - \mathbf{G}) - \hat{N} \right], \quad (56)$$

and \hat{V}_{ext} is the crystal potential, i.e.

$$\hat{V}_{\text{ext}} = \int d^2\mathbf{r} V_{\text{ext}}(\mathbf{r}) \hat{n}(\mathbf{r}) . \quad (57)$$

In Eq. (56), $V(\mathbf{q} + \mathbf{G})$ is the Fourier transform of the electron-electron interaction potential, evaluated at the wave vector $\mathbf{q} + \mathbf{G}$, where \mathbf{q} is in the first BZ and \mathbf{G} is an arbitrary reciprocal lattice vector. Similarly, $\hat{n}(\mathbf{q} + \mathbf{G})$ is the Fourier transform of the ground-state density operator $\hat{n}(\mathbf{r})$.

Let $|\Phi\rangle$ be the ground state of the full Hamiltonian and $n(\mathbf{r})$ the associated ground-state density, i.e.

$$n(\mathbf{r}) = \langle \Phi | \hat{n}(\mathbf{r}) | \Phi \rangle . \quad (58)$$

We now introduce a key auxiliary system, which is described by the so-called *Kohn-Sham Hamiltonian* $\hat{\mathcal{H}}_{\text{KS}}$:

$$\hat{\mathcal{H}}_{\text{KS}} = \hat{T}_e + \hat{V}_{\text{ext}} + \hat{V}_H + \hat{V}_{\text{xc}} \equiv \hat{T}_e + \hat{V}_{\text{KS}} . \quad (59)$$

This Hamiltonian is a (self-consistent) one-particle Hamiltonian whose ground state $|\psi_{\text{KS}}\rangle$ is a Slater determinant of Kohn-Sham orbitals. The fundamental property of this Hamiltonian is that *it yields the exact same density of the full Hamiltonian* (55).

We now define a family $\hat{\mathcal{H}}_\lambda$ of Hamiltonians depending on a real dimensionless parameter $\lambda \in [0, 1]$:

$$\hat{\mathcal{H}}_\lambda = \hat{T}_e + \lambda \hat{\mathcal{H}}_{e-e} + \hat{V}_\lambda . \quad (60)$$

Let $|\psi_\lambda\rangle$ be the normalized ground state of $\hat{\mathcal{H}}_\lambda$, i.e. $\langle \psi_\lambda | \psi_\lambda \rangle = 1 \forall \lambda$. In Eq. (60), \hat{T}_e and $\hat{\mathcal{H}}_{e-e}$ have the exact same meaning as above. The key new quantity is \hat{V}_λ , which is a local potential that interpolates between the Kohn-Sham potential in the limit $\lambda = 0$, i.e. $\hat{V}_{\lambda=0} = \hat{V}_{\text{KS}}$, and the exact, physical crystal potential in the limit $\lambda = 1$, i.e. $\hat{V}_{\lambda=1} = \hat{V}_{\text{ext}}$. Crucially, \hat{V}_λ varies with λ in such a way that the correct electronic density is reproduced at every value of λ , i.e.

$$n_\lambda(\mathbf{r}) \equiv \langle \psi_\lambda | \hat{n}(\mathbf{r}) | \psi_\lambda \rangle = n(\mathbf{r}) \forall \lambda . \quad (61)$$

The uniqueness (up to a constant) of \hat{V}_λ can be proved by applying the Hohenberg-Kohn theorem to the electronic Hamiltonian with reduced coupling constant. In the following, we will fix the arbitrary constant by setting the average value of \hat{V}_λ to zero.

The ground state energy at coupling constant λ is

$$E(\lambda) = \langle \psi_\lambda | \hat{\mathcal{H}}_\lambda | \psi_\lambda \rangle . \quad (62)$$

By applying the Hellman-Feynman theorem we obtain

$$\frac{dE(\lambda)}{d\lambda} = \langle \psi_\lambda | \hat{\mathcal{H}}_{e-e} | \psi_\lambda \rangle + \int d^2\mathbf{r} n(\mathbf{r}) \partial_\lambda V_\lambda(\mathbf{r}) . \quad (63)$$

Integrating the previous differential equation between $\lambda = 0$ and $\lambda = 1$ we find:

$$E(1) - E(0) = \int_0^1 d\lambda \langle \psi_\lambda | \hat{\mathcal{H}}_{e-e} | \psi_\lambda \rangle + \int d^2\mathbf{r} n(\mathbf{r}) [V_{\text{ext}}(\mathbf{r}) - V_{\text{KS}}(\mathbf{r})] . \quad (64)$$

In writing the previous two equations we made use of the crucial fact that $n_\lambda(\mathbf{r}) = n(\mathbf{r})$ for every λ in the integration interval.

We now recall that, in DFT, the exact ground-state energy E of the system, which in the notation of Eq. (64) coincides with $E(1)$, is given by [76]

$$E = E(1) = T_s + \int d^2\mathbf{r} n(\mathbf{r}) V_{\text{ext}}(\mathbf{r}) + E_H + E_{\text{xc}} , \quad (65)$$

where T_s is the non-interacting kinetic energy functional, i.e. the kinetic energy of a non-interacting system whose ground-state density is $n(\mathbf{r})$, E_H is the Hartree energy, i.e.

$$E_H = \frac{1}{2} \int d^2\mathbf{r} \int d^2\mathbf{r}' V(|\mathbf{r} - \mathbf{r}'|) n(\mathbf{r}) n(\mathbf{r}') , \quad (66)$$

and E_{xc} is the exchange-correlation energy functional.

On the other hand, the quantity $E(0)$ is the average of the Kohn-Sham Hamiltonian over the Kohn-Sham ground-state

$$E(0) = \sum_{\alpha \in \text{occ.}} \epsilon_\alpha^{\text{KS}} = T_s + \int d^2\mathbf{r} n(\mathbf{r}) V_{\text{KS}}(\mathbf{r}) , \quad (67)$$

where $\epsilon_\alpha^{\text{KS}}$ are the eigenvalues of the Kohn-Sham equations and the sum runs over the occupied states.

Taking the difference between Eq. (65) and Eq. (67) and comparing the result with Eq. (64) we find the following important result:

$$E_H + E_{\text{xc}} = \int_0^1 d\lambda \langle \psi_\lambda | \hat{\mathcal{H}}_{e-e} | \psi_\lambda \rangle . \quad (68)$$

We can conveniently express the matrix element $\langle \psi_\lambda | \hat{\mathcal{H}}_{e-e} | \psi_\lambda \rangle$ of the interaction Hamiltonian in terms of the density-density response function by using the fluctuation-dissipation theorem [76]. At zero temperature and assuming a non-degenerate ground state, we obtain

$$\begin{aligned} \langle \psi_\lambda | \hat{n}_{\mathbf{q}+\mathbf{G}} \hat{n}_{-\mathbf{q}-\mathbf{G}} | \psi_\lambda \rangle &= -\frac{\hbar}{\pi} \int_0^\infty \text{Im} [\chi_{\hat{n}_{\mathbf{q}+\mathbf{G}} \hat{n}_{-\mathbf{q}-\mathbf{G}}}(\omega, \lambda)] d\omega + \langle \Phi_\lambda | \hat{n}_{\mathbf{q}+\mathbf{G}} | \Phi_\lambda \rangle \langle \Phi_\lambda | \hat{n}_{-\mathbf{q}-\mathbf{G}} | \Phi_\lambda \rangle \\ &= -\frac{\hbar A}{\pi} \int_0^\infty \text{Im} [\chi_{nn}^{\text{GG}}(\mathbf{q}, \omega, \lambda)] d\omega + n_{\mathbf{q}+\mathbf{G}} n_{-\mathbf{q}-\mathbf{G}} . \end{aligned} \quad (69)$$

Making use of (69) and (56) we get

$$\langle \psi_\lambda | \hat{\mathcal{H}}_{e-e} | \psi_\lambda \rangle = \frac{N}{2} \sum_{\mathbf{G}} \int_{\text{BZ}} \frac{d^2\mathbf{q}}{(2\pi)^2} V_{\mathbf{q}+\mathbf{G}} \left\{ \frac{n_{\mathbf{q}+\mathbf{G}} n_{-\mathbf{q}-\mathbf{G}}}{N} - \frac{\hbar}{n\pi} \int_0^\infty d\omega \text{Im} [\chi_{nn}^{\text{GG}}(\mathbf{q}, \omega, \lambda)] - 1 \right\} . \quad (70)$$

The first term is independent of λ and coincides with the Hartree energy,

$$E_H = \frac{1}{2A} \sum_{\mathbf{G} \neq 0} V_{\mathbf{G}} n_{\mathbf{G}} n_{-\mathbf{G}} . \quad (71)$$

We are therefore left with

$$E_{\text{xc}} = \int_0^1 d\lambda \frac{N}{2} \sum_{\mathbf{G}} \int \frac{d^2\mathbf{q}}{(2\pi)^2} V_{\mathbf{q}+\mathbf{G}} \left\{ -\frac{\hbar}{n\pi} \int_0^\infty d\omega \text{Im} [\chi_{nn}^{\text{GG}}(\mathbf{q}, \omega, \lambda)] - 1 \right\} . \quad (72)$$

It can be further shown that the exchange energy can be written as

$$E_x = \frac{N}{2} \sum_{\mathbf{G}} \int \frac{d^2\mathbf{q}}{(2\pi)^2} V_{\mathbf{q}+\mathbf{G}} \left\{ -\frac{\hbar}{n\pi} \int_0^\infty d\omega \text{Im}[\chi_{\text{KS}}^{\mathbf{G}\mathbf{G}}(\mathbf{q}, \omega)] - 1 \right\}, \quad (73)$$

where $\chi_{\text{KS}}^{\mathbf{G}\mathbf{G}}(\mathbf{q}, \omega)$ is the Kohn-Sham response function. Note that this is the exchange energy calculated on the KS orbitals, which is *different* from the Hartree-Fock exchange.

The difference between E_{xc} and E_x is the correlation energy:

$$E_c = \frac{N}{2} \int_0^1 d\lambda \sum_{\mathbf{G}} \int_{\text{BZ}} \frac{d^2\mathbf{q}}{(2\pi)^2} V_{\mathbf{q}+\mathbf{G}} \left\{ -\frac{\hbar}{n\pi} \int_0^\infty d\omega \text{Im}[\chi_{nm}^{\mathbf{G}\mathbf{G}}(\mathbf{q}, \omega, \lambda) - \chi_{\text{KS}}^{\mathbf{G}\mathbf{G}}(\mathbf{q}, \omega)] \right\}. \quad (74)$$

In a crystal, the linear response relation—see Eq. (7.182) in Ref. [76]—relating the full density response at coupling constant λ to the Kohn-Sham density response reads as following:

$$\delta n_{\mathbf{q}+\mathbf{G}}(\omega) = \sum_{\mathbf{G}'} \chi_{\text{KS}}^{\mathbf{G}\mathbf{G}'}(\mathbf{q}, \omega) \left\{ V_{\mathbf{q}+\mathbf{G}'}^{\text{ext}}(\omega) + \sum_{\mathbf{G}''} [\lambda V_{\mathbf{q}+\mathbf{G}'} \delta_{\mathbf{G}'\mathbf{G}''} + f_{\text{xc,L}}^{\mathbf{G}'\mathbf{G}''}(\mathbf{q}, \omega, \lambda)] \delta n_{\mathbf{q}+\mathbf{G}''}(\omega) \right\}, \quad (75)$$

where $f_{\text{xc,L}}^{\mathbf{G}'\mathbf{G}''}(\mathbf{q}, \omega, \lambda)$ is the wave vector and frequency-dependent exchange-correlation kernel [76] evaluate at coupling constant λ . Treating functions in Eq. (75) as matrices with respect to reciprocal lattice vectors indices, we can finally rewrite Eq. (75) as

$$\delta n = \chi_{\text{KS}} \cdot \{V^{\text{ext}} + [\lambda V + f_{\text{xc,L}}(\lambda)] \cdot \delta n\}. \quad (76)$$

Using the same notation, the definition of the full response function at coupling constant λ reads as following:

$$\delta n = \chi(\lambda) \cdot V^{\text{ext}}. \quad (77)$$

Substituting this definition into Eq. (76) yields

$$\chi(\lambda) = \chi_{\text{KS}} \cdot \{1 + [\lambda V + f_{\text{xc,L}}(\lambda)] \cdot \chi(\lambda)\}. \quad (78)$$

Carrying out some simple algebraic manipulation we finally find

$$\chi(\lambda) = \chi_{\text{KS}} \cdot \{1 - [\lambda V + f_{\text{xc,L}}(\lambda)] \cdot \chi_{\text{KS}}\}^{-1}, \quad (79)$$

which can be further rearranged into

$$\chi(\lambda) - \chi_{\text{KS}} = \chi_{\text{KS}} \cdot [\lambda V + f_{\text{xc,L}}(\lambda)] \cdot \chi_{\text{KS}} \cdot \{1 - [\lambda V + f_{\text{xc,L}}(\lambda)] \cdot \chi_{\text{KS}}\}^{-1}. \quad (80)$$

Substituting into the formula for the correlation energy we get the exact expression

$$E_c = -\frac{\hbar N}{2\pi n} \int_{\text{BZ}} \frac{d^2\mathbf{q}}{(2\pi)^2} \int_0^\infty d\omega \int_0^1 d\lambda \text{Im} \left\{ [V \cdot \chi_{\text{KS}} \cdot [\lambda V + f_{\text{xc,L}}(\lambda)] \cdot \chi_{\text{KS}} \cdot [1 - (\lambda V + f_{\text{xc,L}}(\lambda)) \cdot \chi_{\text{KS}}]^{-1}] (\mathbf{q}, \omega) \right\}. \quad (81)$$

The total energy is finally given by

$$E = \sum_{\alpha \in \text{occ.}} \epsilon_{\alpha}^{\text{KS}} - \int d^2\mathbf{r} n(\mathbf{r}) V_{\text{xc}}(\mathbf{r}) - E_{\text{H}} + E_x + E_c. \quad (82)$$

B. Taking the RPA limit

The RPA is obtained by setting to zero \hat{V}_{xc} in the KS equations and $f_{\text{xc,L}}$ in (81). In this limit, the KS equations become the Hartree equations, the KS orbitals become the Hartree orbitals, and the KS response function becomes the Hartree response function.

The coupling-constant integral can then be done analytically, yielding

$$\begin{aligned} E_{c,\text{RPA}} &= -\frac{\hbar N}{2\pi n} \int \frac{d^2\mathbf{q}}{(2\pi)^2} \int_0^\infty d\omega \int_0^1 d\lambda \text{Im} \left\{ \text{Tr} \left[[V \cdot \chi_{\text{H}}]^2 \cdot [1 - \lambda V \cdot \chi_{\text{H}}]^{-1} \right] (\mathbf{q}, \omega) \right\} \\ &= -\frac{\hbar N}{2\pi n} \int \frac{d^2\mathbf{q}}{(2\pi)^2} \int_0^\infty d\omega \int_0^1 d\lambda \text{Im} \left\{ \text{Tr} \left[(\sqrt{V} \cdot \chi_{\text{H}} \cdot \sqrt{V})^2 \cdot (1 - \lambda \sqrt{V} \cdot \chi_{\text{H}} \cdot \sqrt{V})^{-1} \right] (\mathbf{q}, \omega) \right\} \\ &= \frac{N}{2n} \int \frac{d^2\mathbf{q}}{(2\pi)^2} \int_0^\infty \frac{\hbar d\omega}{\pi} \text{Im} \left\{ \text{Tr} \left[\sqrt{V} \cdot \chi_{\text{H}} \cdot \sqrt{V} + \ln(1 - \sqrt{V} \cdot \chi_{\text{H}} \cdot \sqrt{V}) \right] (\mathbf{q}, \omega) \right\}. \end{aligned} \quad (83)$$

Setting $\hat{V}_{xc} = 0$ in (82) we obtain the final expression for the RPA (or time-dependent Hartree) ground-state energy of an inhomogeneous system,

$$E = \sum_{\alpha}^{\text{occ.}} \epsilon_{\alpha}^{\text{H}} - E_{\text{H}} + E_{\text{x}} + E_{\text{c,RPA}}. \quad (84)$$

Note that the Hartree and exchange energies are now calculated on the Hartree orbitals. The first two terms in the previous equation coincide with the Hartree expression of the ground-state energy, avoiding double counting of the Coulomb interaction energy.

VII. THE EXCHANGE-CORRELATION ENERGY OF TBG

Following the ACFDT in SM VI, the exchange-correlation energy of TBG is,

$$\begin{aligned} E_{xc} &= \frac{n}{2} \sum'_{\mathbf{q}, \mathbf{g}} V(\mathbf{q} + \mathbf{g}) \left[-\frac{1}{\pi n} \int_0^1 d\lambda \int_0^{\infty} \text{Im} \chi^{\mathbf{g}\mathbf{g}'}(\mathbf{q}, \omega; \lambda) d\omega - 1 \right] \\ &= \frac{n}{2} \sum'_{\mathbf{q}, \mathbf{g}} V(\mathbf{q} + \mathbf{g}) \left[-\frac{1}{\pi n} \int_0^1 d\lambda \int_0^{\infty} \text{Re} \chi^{\mathbf{g}\mathbf{g}'}(\mathbf{q}, i\omega; \lambda) d\omega - 1 \right] \\ &= \frac{n}{2} \sum'_{\mathbf{q}, \mathbf{g}} V(\mathbf{q} + \mathbf{g}) \left[-\frac{1}{\pi n} \int_0^1 d\lambda \int_0^{\infty} \chi^{\mathbf{g}\mathbf{g}'}(\mathbf{q}, i\omega; \lambda) d\omega - 1 \right]. \end{aligned} \quad (85)$$

In the last two expressions above, the integral along the real axis is rotated to the imaginary axis using the contour deformation, which is justified below.

The response function can be expressed in the entire complex plane using the spectral representation,

$$\chi(z) = -\frac{1}{\pi} \int_{-\infty}^{\infty} \frac{\text{Im} \chi(\omega)}{z - \omega} d\omega. \quad (86)$$

In TBG, the density response function satisfies (as in Eq. (44))

$$\tilde{\chi}^{\mathbf{g}\mathbf{g}'}(\mathbf{q}, \omega) = [\tilde{\chi}^{-\mathbf{g}-\mathbf{g}'}(-\mathbf{q}, -\omega)]^*, \quad (87)$$

therefore

$$\begin{aligned} \tilde{\chi}^{\mathbf{g}\mathbf{g}'}(\mathbf{q}, z) &= -\frac{1}{\pi} \int_0^{\infty} \left[\frac{\text{Im} \tilde{\chi}^{\mathbf{g}\mathbf{g}'}(\mathbf{q}, -\omega)}{z + \omega} + \frac{\text{Im} \tilde{\chi}^{\mathbf{g}\mathbf{g}'}(\mathbf{q}, \omega)}{z - \omega} \right] d\omega \\ &= -\frac{1}{\pi} \int_0^{\infty} \left[\frac{-\text{Im} \tilde{\chi}^{-\mathbf{g}-\mathbf{g}'}(-\mathbf{q}, \omega)}{z + \omega} + \frac{\text{Im} \tilde{\chi}^{\mathbf{g}\mathbf{g}'}(\mathbf{q}, \omega)}{z - \omega} \right] d\omega, \\ \tilde{\chi}^{-\mathbf{g}-\mathbf{g}'}(-\mathbf{q}, z) &= -\frac{1}{\pi} \int_0^{\infty} \left[\frac{\text{Im} \tilde{\chi}^{-\mathbf{g}-\mathbf{g}'}(-\mathbf{q}, -\omega)}{z + \omega} + \frac{\text{Im} \tilde{\chi}^{-\mathbf{g}-\mathbf{g}'}(-\mathbf{q}, \omega)}{z - \omega} \right] d\omega \\ &= -\frac{1}{\pi} \int_0^{\infty} \left[\frac{-\text{Im} \tilde{\chi}^{\mathbf{g}\mathbf{g}'}(\mathbf{q}, \omega)}{z + \omega} + \frac{\text{Im} \tilde{\chi}^{-\mathbf{g}-\mathbf{g}'}(-\mathbf{q}, \omega)}{z - \omega} \right] d\omega. \end{aligned} \quad (88)$$

Combine $\tilde{\chi}^{\mathbf{g}\mathbf{g}'}(\mathbf{q}, z)$ and $\tilde{\chi}^{-\mathbf{g}-\mathbf{g}'}(-\mathbf{q}, z)$,

$$\begin{aligned} \tilde{\chi}^{\mathbf{g}\mathbf{g}'}(\mathbf{q}, z) + \tilde{\chi}^{-\mathbf{g}-\mathbf{g}'}(-\mathbf{q}, z) &= -\frac{1}{\pi} \int_0^{\infty} \left(\text{Im} \tilde{\chi}^{\mathbf{g}\mathbf{g}'}(\mathbf{q}, \omega) + \text{Im} \tilde{\chi}^{-\mathbf{g}-\mathbf{g}'}(-\mathbf{q}, \omega) \right) \left(\frac{1}{z - \omega} - \frac{1}{z + \omega} \right) d\omega \\ &= -\frac{1}{\pi} \int_0^{\infty} \left(\text{Im} \tilde{\chi}^{\mathbf{g}\mathbf{g}'}(\mathbf{q}, \omega) + \text{Im} \tilde{\chi}^{-\mathbf{g}-\mathbf{g}'}(-\mathbf{q}, \omega) \right) \frac{2\omega(z_1^2 - z_2^2 - \omega^2) - i4z_1 z_2 \omega}{(z_1^2 + z_2^2 - \omega^2)^2 + 4z_2^2 \omega^2} d\omega, \end{aligned} \quad (89)$$

where $z = z_1 + iz_2$. Along the imaginary axis, the imaginary part of Eq. (89) vanishes. Therefore the integral along the real axis can be rotated to the imaginary axis:

$$\begin{aligned} \int_0^\infty \left(\tilde{\chi}^{\mathbf{g}\mathbf{g}'}(\mathbf{q}, i\omega) + \tilde{\chi}^{-\mathbf{g}-\mathbf{g}'}(-\mathbf{q}, i\omega) \right) d\omega &= \int_0^\infty \operatorname{Re} \left(\tilde{\chi}^{\mathbf{g}\mathbf{g}'}(\mathbf{q}, i\omega) + \tilde{\chi}^{-\mathbf{g}-\mathbf{g}'}(-\mathbf{q}, i\omega) \right) d\omega \\ &= \int_0^\infty \operatorname{Im} \left(\tilde{\chi}^{\mathbf{g}\mathbf{g}'}(\mathbf{q}, \omega) + \tilde{\chi}^{-\mathbf{g}-\mathbf{g}'}(-\mathbf{q}, \omega) \right) d\omega \end{aligned} \quad (90)$$

Return to the xc energy, since only the diagonal in \mathbf{g} elements of matrix $\chi(\mathbf{q}, i\omega; \lambda)$ is relevant in Eq. (85), and the Coulomb matrix $\mathbf{V}(\mathbf{q})$ is diagonal in \mathbf{g} , the exchange-correlation energy can also be written in the matrix product form,

$$E_{xc} = \frac{n}{2} \sum_{\mathbf{q}} \left[-\frac{1}{\pi n} \int_0^1 d\lambda \int_0^\infty d\omega \operatorname{Tr}(\mathbf{V}(\mathbf{q})\chi(\mathbf{q}, i\omega; \lambda)) - \operatorname{Tr}(\mathbf{V}(\mathbf{q})) \right]. \quad (91)$$

The coupling-constant-dependent density response function in Eq. (85) and Eq. (91) is approximated, within the RPA, with

$$\begin{aligned} \chi(\lambda) &= \tilde{\chi}_H (1 - \lambda V \tilde{\chi}_H)^{-1} \\ &= \tilde{\chi}_H + \lambda \tilde{\chi}_H V \tilde{\chi}_H (1 - \lambda V \tilde{\chi}_H)^{-1}, \end{aligned} \quad (92)$$

where $\tilde{\chi}_H$ is the proper density response function of the self-consistent Hartree approximation. The expression of $\tilde{\chi}_H$ of a specific flavor is shown in Eq. (49).

The exchange energy E_x is the first order contribution in Eq. (85) and Eq. (91), *i.e.* arising from the first term in Eq. (92)

$$\begin{aligned} E_x &= \frac{n}{2} \sum_{\mathbf{q}, \mathbf{g}} V(\mathbf{q} + \mathbf{g}) \left[-\frac{1}{\pi n} \int_0^\infty \tilde{\chi}_H^{\mathbf{g}\mathbf{g}}(\mathbf{q}, i\omega) d\omega - 1 \right] \\ &= \frac{n}{2} \sum_{\mathbf{q}} \left[-\frac{1}{\pi n} \operatorname{Tr}(\mathbf{V}(\mathbf{q})\tilde{\chi}_H(\mathbf{q})) - \operatorname{Tr}(\mathbf{V}(\mathbf{q})) \right]. \end{aligned} \quad (93)$$

Using the Lindhard formula, the diagonal elements of $\tilde{\chi}_H$ is

$$\tilde{\chi}_H^{\mathbf{g}\mathbf{g}}(\mathbf{q}, i\omega) = \frac{1}{A} \sum_{n, m, \mathbf{k}} \left(\frac{\varepsilon_{n\mathbf{k}} - \varepsilon_{m\mathbf{k}+\mathbf{q}}}{\omega^2 + (\varepsilon_{n\mathbf{k}} - \varepsilon_{m\mathbf{k}+\mathbf{q}})^2} - i \frac{\omega}{\omega^2 + (\varepsilon_{n\mathbf{k}} - \varepsilon_{m\mathbf{k}+\mathbf{q}})^2} \right) (f_{n\mathbf{k}} - f_{m\mathbf{k}+\mathbf{q}}) \left| \sum_{\alpha, \mathbf{g}_1} z_{\alpha, \mathbf{g}_1}^n(\mathbf{k}) \bar{z}_{\alpha, \mathbf{g}_1+\mathbf{g}}^m(\mathbf{k} + \mathbf{q}) \right|^2 \quad (94)$$

and its real and imaginary parts are respectively

$$\begin{aligned} \operatorname{Re} \tilde{\chi}_H^{\mathbf{g}\mathbf{g}}(\mathbf{q}, i\omega) &= \frac{1}{A} \sum_{n, m, \mathbf{k}} \frac{(\varepsilon_{n\mathbf{k}} - \varepsilon_{m\mathbf{k}+\mathbf{q}})(f_{n\mathbf{k}} - f_{m\mathbf{k}+\mathbf{q}})}{\omega^2 + (\varepsilon_{n\mathbf{k}} - \varepsilon_{m\mathbf{k}+\mathbf{q}})^2} \left| \sum_{\alpha, \mathbf{g}_1} z_{\alpha, \mathbf{g}_1}^n(\mathbf{k}) \bar{z}_{\alpha, \mathbf{g}_1+\mathbf{g}}^m(\mathbf{k} + \mathbf{q}) \right|^2, \\ \operatorname{Im} \tilde{\chi}_H^{\mathbf{g}\mathbf{g}}(\mathbf{q}, i\omega) &= -\frac{1}{A} \sum_{n, m, \mathbf{k}} \frac{\omega(f_{n\mathbf{k}} - f_{m\mathbf{k}+\mathbf{q}})}{\omega^2 + (\varepsilon_{n\mathbf{k}} - \varepsilon_{m\mathbf{k}+\mathbf{q}})^2} \left| \sum_{\alpha, \mathbf{g}_1} z_{\alpha, \mathbf{g}_1}^n(\mathbf{k}) \bar{z}_{\alpha, \mathbf{g}_1+\mathbf{g}}^m(\mathbf{k} + \mathbf{q}) \right|^2. \end{aligned} \quad (95)$$

$\varepsilon_{n\mathbf{k}}$, $z^n(\mathbf{k})$ are eigen-energies and eigenvectors of the self-consistent Hartree approximation. Using the integration equality

$$\int_0^\infty d\omega \frac{1}{\omega^2 + a^2} = \frac{1}{a} \arctan \left(\frac{\omega}{a} \right) \Big|_0^\infty = \frac{\pi}{2|a|}, \quad (96)$$

the frequency integration of the real part of $\tilde{\chi}_H^{\mathbf{g}\mathbf{g}}(\mathbf{q}, i\omega)$ can be done analytically:

$$\int_0^\infty \operatorname{Re} \tilde{\chi}_H^{\mathbf{g}\mathbf{g}}(\mathbf{q}, i\omega) d\omega = \frac{\pi}{2A} \sum_{n, m, \mathbf{k}} \frac{(\varepsilon_{n\mathbf{k}} - \varepsilon_{m\mathbf{k}+\mathbf{q}})(f_{n\mathbf{k}} - f_{m\mathbf{k}+\mathbf{q}})}{|\varepsilon_{n\mathbf{k}} - \varepsilon_{m\mathbf{k}+\mathbf{q}}|} \langle n\mathbf{k} | e^{-i(\mathbf{q}+\mathbf{g}) \cdot \mathbf{r}} | m\mathbf{k} + \mathbf{q} \rangle \langle m\mathbf{k} + \mathbf{q} | e^{i(\mathbf{q}+\mathbf{g}) \cdot \mathbf{r}} | n\mathbf{k} \rangle. \quad (97)$$

Rewrite the Fermi-Dirac occupation difference

$$f_{n\mathbf{k}} - f_{m\mathbf{k}+\mathbf{q}} = f_{n\mathbf{k}}(1 - f_{m\mathbf{k}+\mathbf{q}}) - (1 - f_{n\mathbf{k}})f_{m\mathbf{k}+\mathbf{q}} \quad (98)$$

and it is clear that

$$\frac{\varepsilon_{n\mathbf{k}} - \varepsilon_{m\mathbf{k}+\mathbf{q}}}{|\varepsilon_{n\mathbf{k}} - \varepsilon_{m\mathbf{k}+\mathbf{q}}|} = \begin{cases} -1, & \text{if } f_{n\mathbf{k}} = 1 \text{ and } f_{m\mathbf{k}+\mathbf{q}} = 0, \\ 1, & \text{if } f_{n\mathbf{k}} = 0 \text{ and } f_{m\mathbf{k}+\mathbf{q}} = 1. \end{cases} \quad (99)$$

Then Eq. (97) becomes

$$\begin{aligned} \int_0^\infty \text{Re} \tilde{\chi}_H^{\mathbf{g}\mathbf{g}}(\mathbf{q}, i\omega) d\omega &= -\frac{\pi}{2A} \sum_{n,m,\mathbf{k}} [f_{n\mathbf{k}}(1 - f_{m\mathbf{k}+\mathbf{q}}) + (1 - f_{n\mathbf{k}})f_{m\mathbf{k}+\mathbf{q}}] \langle n\mathbf{k} | e^{-i(\mathbf{q}+\mathbf{g})\cdot\mathbf{r}} | m\mathbf{k} + \mathbf{q} \rangle \langle m\mathbf{k} + \mathbf{q} | e^{i(\mathbf{q}+\mathbf{g})\cdot\mathbf{r}} | n\mathbf{k} \rangle \\ &= -\frac{\pi}{2A} \sum_{n,m,\mathbf{k}} (f_{n\mathbf{k}} + f_{m\mathbf{k}+\mathbf{q}} - 2f_{n\mathbf{k}}f_{m\mathbf{k}+\mathbf{q}}) \langle n\mathbf{k} | e^{-i(\mathbf{q}+\mathbf{g})\cdot\mathbf{r}} | m\mathbf{k} + \mathbf{q} \rangle \langle m\mathbf{k} + \mathbf{q} | e^{i(\mathbf{q}+\mathbf{g})\cdot\mathbf{r}} | n\mathbf{k} \rangle. \end{aligned} \quad (100)$$

The first two terms are simply total occupation number

$$\begin{aligned} \sum_{n,m,\mathbf{k}} f_{n\mathbf{k}} \langle n\mathbf{k} | e^{-i(\mathbf{q}+\mathbf{g})\cdot\mathbf{r}} | m\mathbf{k} + \mathbf{q} \rangle \langle m\mathbf{k} + \mathbf{q} | e^{i(\mathbf{q}+\mathbf{g})\cdot\mathbf{r}} | n\mathbf{k} \rangle &= \sum_{n,\mathbf{k}} f_{n\mathbf{k}} = N, \\ \sum_{n,m,\mathbf{k}} f_{m\mathbf{k}+\mathbf{q}} \langle n\mathbf{k} | e^{-i(\mathbf{q}+\mathbf{g})\cdot\mathbf{r}} | m\mathbf{k} + \mathbf{q} \rangle \langle m\mathbf{k} + \mathbf{q} | e^{i(\mathbf{q}+\mathbf{g})\cdot\mathbf{r}} | n\mathbf{k} \rangle &= \sum_{m,\mathbf{k}} f_{m\mathbf{k}+\mathbf{q}} = N. \end{aligned} \quad (101)$$

Equation (100) becomes

$$\int_0^\infty \text{Re} \tilde{\chi}_H^{\mathbf{g}\mathbf{g}}(\mathbf{q}, i\omega) d\omega = -\pi n + \frac{\pi}{A} \sum_{n,m,\mathbf{k}} f_{n\mathbf{k}} f_{m\mathbf{k}+\mathbf{q}} \langle n\mathbf{k} | e^{-i(\mathbf{q}+\mathbf{g})\cdot\mathbf{r}} | m\mathbf{k} + \mathbf{q} \rangle \langle m\mathbf{k} + \mathbf{q} | e^{i(\mathbf{q}+\mathbf{g})\cdot\mathbf{r}} | n\mathbf{k} \rangle. \quad (102)$$

Substitute into the exchange energy Eq. (93), the $-\pi n$ term above cancels exactly with the self-interacting term, and the exchange energy is simply

$$\begin{aligned} E_x &= -\frac{1}{2A} \sum'_{\mathbf{q},\mathbf{g}} V(\mathbf{q} + \mathbf{g}) \sum_{n,m,\mathbf{k}} f_{n\mathbf{k}} f_{m\mathbf{k}+\mathbf{q}} \left| \sum_{\alpha,\mathbf{g}_1} z_{\alpha,\mathbf{g}_1}^n(\mathbf{k}) \bar{z}_{\alpha,\mathbf{g}_1+\mathbf{g}}^m(\mathbf{k} + \mathbf{q}) \right|^2 \\ &= -\frac{1}{2A} \sum'_{\mathbf{q},\mathbf{g}} V(\mathbf{q} + \mathbf{g}) \sum_{n,m,\mathbf{k}} f_{n\mathbf{k}} f_{m\mathbf{k}+\mathbf{q}} \sum_{\alpha,\beta,\mathbf{g}_1,\mathbf{g}_2} \bar{\rho}_{\alpha,\mathbf{g}_1;\beta,\mathbf{g}_2}^n(\mathbf{k}) \rho_{\alpha,\mathbf{g}_1+\mathbf{g};\beta,\mathbf{g}_2+\mathbf{g}}^m(\mathbf{k} + \mathbf{q}). \end{aligned} \quad (103)$$

This exchange energy looks like the HF exchange but it is not since it is calculated over the SCH wavefunctions instead of the self-consistent HF wavefunctions.

On the other hand, the correlation energy is given by higher order contributions in RPA. Use

$$\text{Tr}(\mathbf{V}\chi) = \text{Tr}(\sqrt{\mathbf{V}}\chi\sqrt{\mathbf{V}}), \quad (104)$$

the correlation energy is

$$\begin{aligned} E_c &= -\frac{1}{2\pi} \sum'_{\mathbf{q}} \int_0^1 d\lambda \int_0^\infty d\omega \text{Tr}[\lambda(\sqrt{\mathbf{V}}\tilde{\chi}_H\sqrt{\mathbf{V}})^2(1 - \lambda\sqrt{\mathbf{V}}\tilde{\chi}_H\sqrt{\mathbf{V}})^{-1}] \\ &= \frac{1}{2\pi} \sum'_{\mathbf{q}} \int_0^\infty d\omega \text{Tr}[\sqrt{\mathbf{V}}\tilde{\chi}_H\sqrt{\mathbf{V}} + \ln(1 - \sqrt{\mathbf{V}}\tilde{\chi}_H\sqrt{\mathbf{V}})]. \end{aligned} \quad (105)$$

For any diagonalizable and non-singular (invertible) matrix \mathbf{A} , its logarithm is

$$\ln \mathbf{A} = \mathbf{v}(\ln \lambda)\mathbf{v}^{-1}, \quad (106)$$

where λ is the diagonal matrix of eigenvalues of \mathbf{A} ,

$$\lambda = \mathbf{v}^{-1}\mathbf{A}\mathbf{v}, \quad (107)$$

and \mathbf{v} is the matrix with eigenvectors in each column. The trace of $\ln \mathbf{A}$

$$\begin{aligned} \text{Tr} \ln \mathbf{A} &= \text{Tr}[\mathbf{v}(\ln \lambda)\mathbf{v}^{-1}] \\ &= \text{Tr}[(\ln \lambda)\mathbf{v}^{-1}\mathbf{v}] \\ &= \text{Tr} \ln \lambda \\ &= \ln \det \mathbf{A}. \end{aligned} \quad (108)$$

The correlation energy

$$\begin{aligned}
E_c &= \frac{1}{2\pi} \sum_{\mathbf{q}} \int_0^\infty d\omega \text{Tr} \left[\mathbf{V}(\mathbf{q}) \tilde{\chi}_H(\mathbf{q}, i\omega) + \ln \left(1 - \sqrt{\mathbf{V}(\mathbf{q})} \tilde{\chi}_H(\mathbf{q}, i\omega) \sqrt{\mathbf{V}(\mathbf{q})} \right) \right] \\
&= \frac{1}{2\pi} \sum_{\mathbf{q}} \int_0^\infty d\omega \left[\text{Tr}(\mathbf{V}(\mathbf{q}) \tilde{\chi}_H(\mathbf{q}, i\omega)) + \sum_i \ln \lambda_i(\mathbf{q}, i\omega) \right],
\end{aligned} \tag{109}$$

where $\lambda_i(\mathbf{q}, i\omega)$ is the i -th eigenvalue of $(1 - \sqrt{\mathbf{V}} \tilde{\chi}_H \sqrt{\mathbf{V}})$.

VIII. EXCHANGE ENERGY REGULARIZATION

The exchange energy in Eq. (103) must be regularized to deal with the negative energy sea of the Dirac model. In the main text we denote E_x as the regularized exchange energy

$$\begin{aligned}
E_x &= -\frac{1}{2A} \sum_{\mathbf{q}, \mathbf{g}} V(\mathbf{q} + \mathbf{g}) \sum_{\substack{\mathbf{k}, \mathbf{g}_1, \mathbf{g}_2 \\ \alpha, \beta}} \left[\bar{\rho}_{\alpha, \mathbf{g}_1; \beta, \mathbf{g}_2}(\mathbf{k}) \rho_{\alpha, \mathbf{g}_1 + \mathbf{g}; \beta, \mathbf{g}_2 + \mathbf{g}}(\mathbf{k} + \mathbf{q}) - \bar{\rho}_{\alpha, \mathbf{g}_1; \beta, \mathbf{g}_2}^0(\mathbf{k}) \rho_{\alpha, \mathbf{g}_1 + \mathbf{g}; \beta, \mathbf{g}_2 + \mathbf{g}}^0(\mathbf{k} + \mathbf{q}) \right] \\
&= -\frac{1}{2A} \sum_{\mathbf{q}, \mathbf{g}} V(\mathbf{q} + \mathbf{g}) \sum_{\substack{\mathbf{k}, \mathbf{g}_1, \mathbf{g}_2 \\ \alpha, \beta}} \left[\delta \bar{\rho}(\mathbf{k}) + 2\bar{\rho}^0(\mathbf{k}) \right]_{\alpha, \mathbf{g}_1; \beta, \mathbf{g}_2} \delta \rho_{\alpha, \mathbf{g}_1 + \mathbf{g}; \beta, \mathbf{g}_2 + \mathbf{g}}(\mathbf{k} + \mathbf{q}).
\end{aligned} \tag{110}$$

ρ^0 is the density matrix of the charge neutral decoupled bilayer and therefore it's diagonal in \mathbf{g} 's:

$$\rho_{\alpha, \mathbf{g}_1; \beta, \mathbf{g}_2}^0(\mathbf{k}) = \delta_{\mathbf{g}_1 \mathbf{g}_2} \sum_{n \in \mathcal{V}} z_{n, \alpha, \mathbf{g}_1}^0(\mathbf{k}) \bar{z}_{n, \beta, \mathbf{g}_2}^0(\mathbf{k}). \tag{111}$$

Summing over two valence bands from top and bottom layer Dirac cones, the 4×4 density matrix with an explicit \mathbf{g} is

$$\rho_{\mathbf{g}; \mathbf{g}}^0(\mathbf{k}) \equiv \rho^0(\mathbf{k} + \mathbf{g}) = \frac{1}{2} \begin{pmatrix} 1 & -e^{-i(\theta_{\mathbf{k}+\mathbf{g}-\mathbf{K}_1}-\theta/2)} & 0 & 0 \\ -e^{i(\theta_{\mathbf{k}+\mathbf{g}-\mathbf{K}_1}-\theta/2)} & 1 & 0 & 0 \\ 0 & 0 & 1 & -e^{-i(\theta_{\mathbf{k}+\mathbf{g}-\mathbf{K}_2}+\theta/2)} \\ 0 & 0 & -e^{i(\theta_{\mathbf{k}+\mathbf{g}-\mathbf{K}_2}+\theta/2)} & 1 \end{pmatrix}. \tag{112}$$

Therefore, the second part of the second line of Eq. (110) is equivalent to

$$E_x^{(2)} = -\frac{1}{A} \sum_{\substack{\mathbf{k}' \in \text{MBZ} \\ \mathbf{k} \in k_c \sim 1/a}} V(\mathbf{k}' - \mathbf{k} + \mathbf{g}) \sum_{\mathbf{g}_1, \alpha, \beta} \bar{\rho}_{\alpha \beta}^0(\mathbf{k} + \mathbf{g}_1) \delta \rho_{\alpha, \mathbf{g}_1 + \mathbf{g}; \beta, \mathbf{g}_1 + \mathbf{g}}(\mathbf{k}') \tag{113}$$

Because the diagonal terms of ρ^0 contribute a constant energy shift which is proportional to the occupation number at \mathbf{k}' , only off-diagonal terms of ρ^0 matter and it's

$$\begin{aligned}
E_x^{(2)} &= \frac{2\pi e^2}{\epsilon} \frac{1}{8\pi} \sum_{\mathbf{k}' \in \text{MBZ}, \mathbf{g}} \left[e^{i\xi(\theta_{\mathbf{k}'+\mathbf{g}-\mathbf{K}_1}-\theta/2)} [\delta \rho_{\mathbf{g}; \mathbf{g}}]_{12}(\mathbf{k}') |\mathbf{k}' + \mathbf{g} - \mathbf{K}_1| \ln \frac{k_c}{|\mathbf{k}' + \mathbf{g} - \mathbf{K}_1|} \right. \\
&\quad \left. + e^{i\xi(\theta_{\mathbf{k}'+\mathbf{g}-\mathbf{K}_2}+\theta/2)} \delta [\rho_{\mathbf{g}; \mathbf{g}}]_{34}(\mathbf{k}') |\mathbf{k}' + \mathbf{g} - \mathbf{K}_2| \ln \frac{k_c}{|\mathbf{k}' + \mathbf{g} - \mathbf{K}_2|} + h.c \right]
\end{aligned} \tag{114}$$

Therefore the regularized exchange energy is

$$E_x = -\frac{1}{2A} \sum_{\mathbf{q}, \mathbf{g}} V(\mathbf{q} + \mathbf{g}) \sum_{\substack{\mathbf{k}, \mathbf{g}_1, \mathbf{g}_2 \\ \alpha, \beta}} \delta \bar{\rho}_{\alpha, \mathbf{g}_1; \beta, \mathbf{g}_2}(\mathbf{k}) \delta \rho_{\alpha, \mathbf{g}_1 + \mathbf{g}; \beta, \mathbf{g}_2 + \mathbf{g}}(\mathbf{k} + \mathbf{q}) + E_x^{(2)}. \tag{115}$$

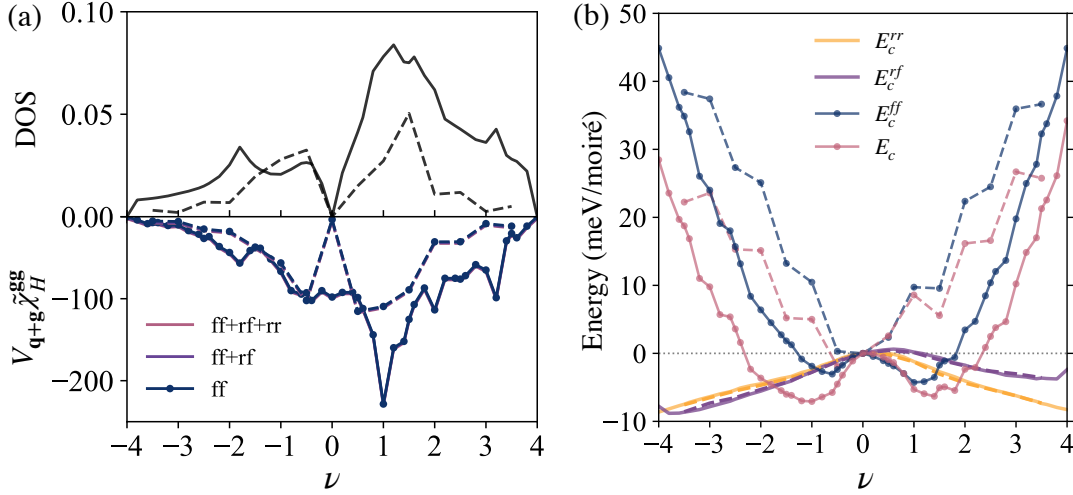


FIG. 7. (a) Density of state in unit of $\text{meV}^{-1}\cdot\text{nm}^{-2}$ and $V_{\mathbf{q}+\mathbf{g}}\tilde{\chi}_H^{gg}(\mathbf{q}, i\omega=0)$ as a function of ν , with $\mathbf{g}=0$ and $\mathbf{q}=(-\sqrt{3}/2, -1/2)g_M/\sqrt{3}$, where g_M is the length of moiré primitive reciprocal lattice vector. Different colors in $V_{\mathbf{q}+\mathbf{g}}\tilde{\chi}_H^{gg}(\mathbf{q}, i\omega=0)$ plot label distinct particle-hole excitations as indicated by the legend. (a) shows that excitations between flat bands (ff) dominate when the flat bands are not empty or fully occupied. (b) The correlation energy E_c as a function of ν . E_c^{ff} , E_c^{rf} and E_c^{rr} are contributions to the correlation energy from excitations between flat bands, between remote and flat bands and between remote bands respectively. E_c^{rr} and E_c^{rf} are independent of flavor polarizations. In both figures, solid lines represent flavor paramagnetic states and dashed lines represent flavor fully polarized states, for example at $\nu=2$, $\nu_f=(1, 1, 0, 0)$.

IX. SCREENING EFFECTS FROM REMOTE BANDS

In Fig. 7(a) we show the density of state (DOS) and $V_{\mathbf{q}+\mathbf{g}}\tilde{\chi}_H^{gg}(\mathbf{q}, i\omega=0)$ as a function of ν , for the specific \mathbf{g} and \mathbf{q} . For both flavor paramagnetic state (solid lines) and flavor polarized state (dashed lines), electron-hole excitations between flat bands (ff) dominate over excitations between remote and flat bands (rf) and between remote bands (rr), as long as flat bands are not entirely empty or fully occupied. In Fig. 7(b), contributions to the correlation energy (E_c) from electron-hole excitations between flat bands (E_c^{ff}), between remote and flat bands (E_c^{rf}) and between remote bands (E_c^{rr}) are separately shown. E_c^{ff} dominates and is responsible for the tendency of E_c with respect to ν . By comparing correlation energies of flavor paramagnetic state (solid lines) with flavor polarized state (dashed lines), E_c^{rr} and E_c^{rf} are almost independent of flavor polarizations.

Figure 8 shows $V_{\mathbf{q}+\mathbf{g}}\tilde{\chi}_H^{gg}(\mathbf{q}, i\omega)$ at $\nu=-1$ as a function of frequency, for the specific \mathbf{g} and \mathbf{q} . It illustrates that the xc energy are dominated by diagonal elements of $\mathbf{V}\tilde{\chi}_H$ with the smallest $|\mathbf{g}|$ and by excitations between flat bands (ff).

Figure 9 shows the sum of eigenvalues of $\ln(1-\mathbf{V}\tilde{\chi})$, *i.e.* the second term of Eq. (5), as a function of q and unitless frequency $\tilde{\omega}$. Again the correlation effect is dominated by ff excitations.

X. ENERGIES OF COMPETING BROKEN FLAVOR-SYMMETRY STATES

Figure 10 schematically summarizes our findings in Table I by plotting the total energy (Fig. 10(a)) and xc energy (Fig. 10(b)) relative to the flavor paramagnetic state for various flavor polarizations (y -axis) as a function of filling factor ν (x -axis). $E_{tot}^S - E_{tot} > 0$ indicates the ground state favors flavor polarized states. $E_{xc}^S - E_{xc} > 0$ indicates the xc effect, when the single-quasiparticle energy is ignored, favors flavor polarized states. Figure 10(b) clearly shows that the xc effect predicts broken flavor symmetry for $|\nu| \geq 1$ on both electron- and hole-doped sides and is stronger on the electron-doped side. After including the single-quasiparticle energy which in general prefers unpolarized state, however, the ground state is predicted to be flavor paramagnetic on hole-doped side. This is a result of the fact that on the hole-doped side the Hartree energy is twice stronger and the xc effect is weaker than that on the electron-doped side.

We further explore the effects of C_2T symmetry breaking on energies, as summarized in Table II. We find that flavor ferromagnetic states are favored at all filling factors including those near CN, consistent with experiments that hBN alignment favors broken symmetry states.

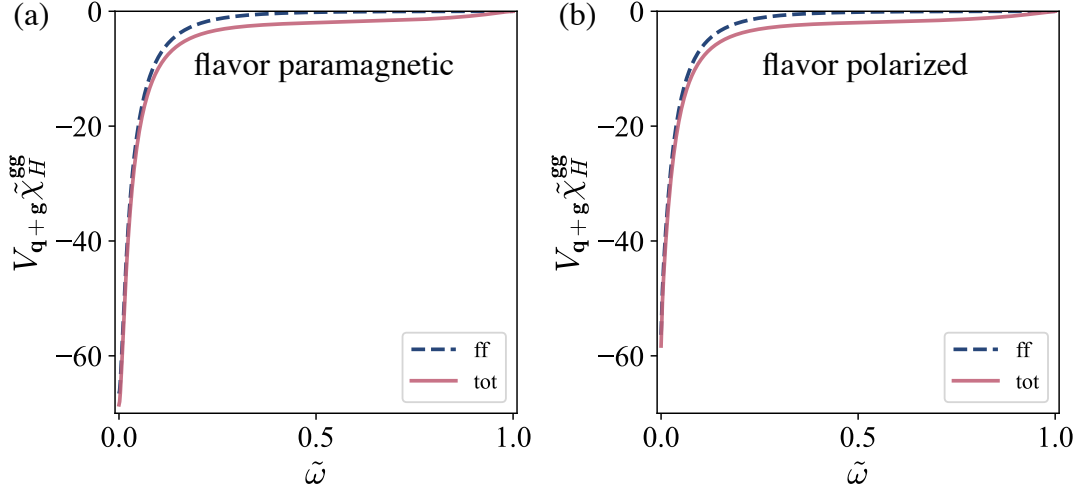


FIG. 8. $V_{\mathbf{q}+\mathbf{g}} \tilde{\chi}_H^{gg}(\mathbf{q}, i\omega)$ at $\nu = -1$ as a function of the unitless frequency $\tilde{\omega}$, with $\mathbf{g} = 0$ and $\mathbf{q} = (-\sqrt{3}/2, -1/2)g_M/\sqrt{3}$. $\tilde{\omega} = \omega/(\omega + \omega_0)$, where $\omega_0 = 30$ meV is chosen to be around the size of flat-band bandwidth. Electron-hole excitations between flat bands (ff) play a dominant role in the correlation effect.

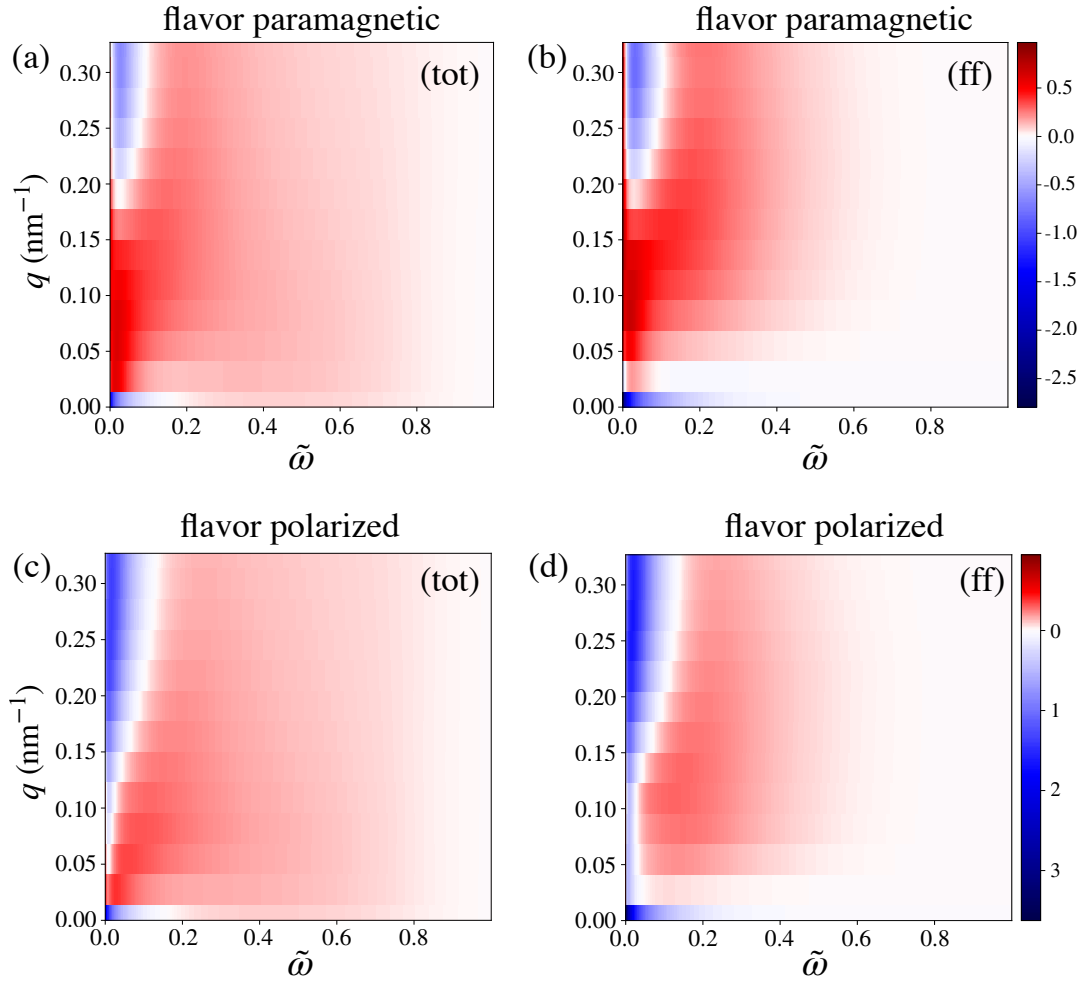


FIG. 9. $\sum_j \ln(1 - |\lambda_j|)$ with respect to q and unitless frequency $\tilde{\omega}$, where λ_j is the j -th eigenvalue of $\mathbf{V} \tilde{\chi}_H$.

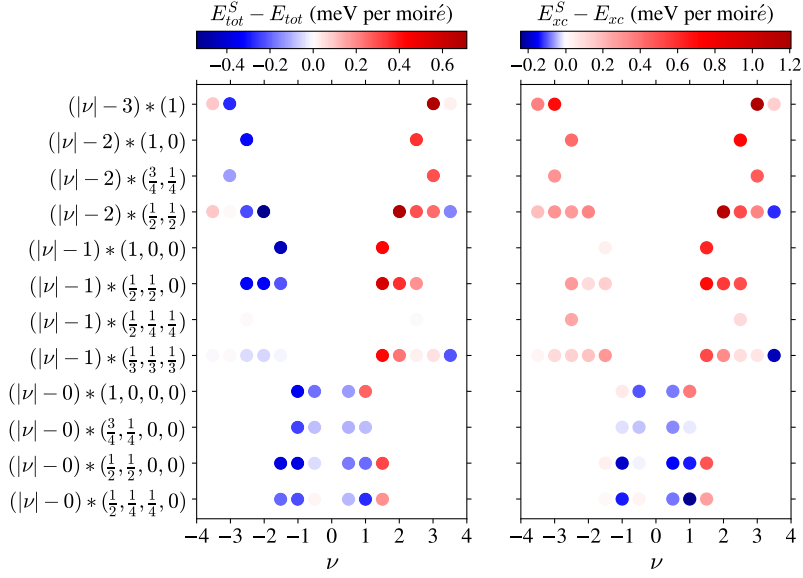


FIG. 10. (a) Total energy E_{tot} and (b) xc energy (E_{xc}) relative to those of the flavor paramagnetic state (E_{tot}^S, E_{xc}^S), for various flavor-polarized states (y-axis) as a function of ν (x-axis). The y-axis is labeled by $(|\nu| - n) * (f_1, \dots)$, where the integer n indicates the number of flavors that are fully occupied or empty and fractions inside the right bracket, multiplied by $(|\nu| - n)$, denote filling factors of the remaining partially occupied flavors. For example, the data point at $\nu = -1$ and $(|\nu| - 0) * (1/2, 1/4, 1/4, 0)$ represents the filling factors of four flavors are $-(1/2, 1/4, 1/4, 0)$ respectively. $E_{tot}^S - E_{tot} > 0$ indicates the ground state favors flavor polarized states and $E_{xc}^S - E_{xc} > 0$ indicates the xc energy favors flavor polarized states.

XI. MAGNETIC ANISOTROPY IN $SU(4)$ FERROMAGNETS

MATBG has $SU(4)$ ferromagnetism because of its four degenerate spin-valley flavors. In the continuum model we employ the $SU(4)$ symmetry is reduced to $SU(2) \times SU(2) \times U(1)$ by the difference between two valley projected band Hamiltonians, which contribute explicitly to the model's $SU(4)$ magnetic anisotropy. Valley-exchange and spin-orbit interactions, which we neglect, also contribute to magnetic anisotropy. In our RPA approach, we neglect anisotropy by focusing only on flavor-dependent filling factors, the eigenvalues of the spin-valley density matrix. Indeed our explicit calculations assume that the ferromagnet's density matrix remains diagonal in the spin-valley representation because total valley occupation number remains a good quantum number, simplifying the use of a coupling-constant integral representation of the energy. There is in fact theoretical [22, 78–81] and experimental [82–85] work that intervalley coherence, which breaks valley number symmetry, is present in many MATBG ferromagnets. Our calculations make no effort to distinguish between ferromagnets that differ only in the orientation of the spin-valley magnetization and not in its magnitude as characterized by the differences between spin-valley density-matrix eigenvalues. There is evidence in recent experiments [85], in the form of the presence of sample-specific domain walls and vortices in various partial order parameters, that as in most conventional ferromagnets the energy scale associated with anisotropy is smaller than the energy scale associated with ordering.

ν	$(\nu_1, \nu_2, \nu_3, \nu_4)$	E_0	E_x	E_c	E_{xc}	E_{tot}	ν	$(\nu_1, \nu_2, \nu_3, \nu_4)$	E_0	E_x	E_c	E_{xc}	E_{tot}
-0.5	(-1/8, -1/8, -1/8, -1/8)	-5.477	6.097	-4.520	1.577	-3.900	0.5	(1/8, 1/8, 1/8, 1/8)	6.852	1.570	-0.930	0.640	7.492
	(-1/4, -1/8, -1/8, 0)	-5.458	5.534	-3.992	1.542	-3.916		(1/4, 1/8, 1/8, 0)	6.864	1.163	-0.443	0.720	7.584
	(-1/4, -1/4, 0, 0)	-5.437	5.417	-3.834	1.583	-3.854		(1/4, 1/4, 0, 0)	6.876	0.756	0.033	0.789	7.665
	(-3/8, -1/8, 0, 0)	-5.426	4.650	-3.039	1.611	-3.815		(3/8, 1/8, 0, 0)	6.882	0.006	0.702	0.708	7.590
	(-1/2, 0, 0, 0)	-5.386	3.586	-1.913	1.673	-3.713		(1/2, 0, 0, 0)	6.905	-1.863	2.579	0.716	7.621
-1.0	(-1/4, -1/4, -1/4, -1/4)	-10.236	11.187	-7.073	4.114	-6.122	1.0	(1/4, 1/4, 1/4, 1/4)	14.774	8.384	-5.293	3.091	17.865
	(-1/2, -1/4, -1/4, 0)	-10.138	9.902	-5.659	4.243	-5.895		(1/2, 1/4, 1/4, 0)	14.806	6.313	-2.983	3.330	18.136
	(-1/2, -1/2, 0, 0)	-10.044	8.465	-4.162	4.303	-5.741		(1/2, 1/2, 0, 0)	14.833	4.721	-1.500	3.221	18.054
	(-3/4, -1/4, 0, 0)	-10.006	6.076	-1.946	4.130	-5.876		(3/4, 1/4, 0, 0)	14.848	1.755	1.349	3.104	17.952
	(-1, 0, 0, 0)	-9.816	-0.957	5.008	4.051	-5.765		(1, 0, 0, 0)	14.907	-5.881	8.586	2.705	17.612
-1.5	(-3/8, -3/8, -3/8, -3/8)	-13.764	11.482	-6.009	5.473	-8.291	1.5	(3/8, 3/8, 3/8, 3/8)	23.162	11.808	-5.054	6.754	29.916
	(-3/4, -3/8, -3/8, 0)	-13.559	7.287	-1.825	5.462	-8.097		(3/4, 3/8, 3/8, 0)	23.239	7.646	-1.159	6.487	29.726
	(-3/4, -3/4, 0, 0)	-13.335	3.008	2.418	5.426	-7.909		(3/4, 3/4, 0, 0)	23.328	3.450	2.815	6.265	29.593
	(-1, -1/6, -1/6, -1/6)	-13.450	1.424	3.749	5.173	-8.277		(1, 1/6, 1/6, 1/6)	23.261	2.345	3.882	6.227	29.488
	(-1, -1/4, -1/4, 0)	-13.410	1.267	4.071	5.338	-8.072		(1, 1/4, 1/4, 0)	23.297	1.984	4.065	6.049	29.346
	(-1, -1/2, 0, 0)	-13.266	0.215	5.212	5.427	-7.839		(1, 1/2, 0, 0)	23.355	0.570	5.556	6.126	29.481
-2.0	(-1/2, -1/2, -1/2, -1/2)	-15.756	9.684	-3.635	6.049	-9.707	2.0	(1/2, 1/2, 1/2, 1/2)	32.588	11.054	-2.341	8.713	41.301
	(-1, -1/3, -1/3, -1/3)	-15.530	1.340	4.537	5.877	-9.653		(1, 1/3, 1/3, 1/3)	32.681	4.395	3.984	8.379	41.060
	(-1, -1/2, -1/2, 0)	-15.314	0.227	5.721	5.948	-9.366		(1, 1/2, 1/2, 0)	32.793	1.151	6.991	8.142	40.935
	(-1, -1, 0, 0)	-14.862	-9.434	15.127	5.693	-9.169		(1, 1, 0, 0)	32.985	-8.577	16.158	7.581	40.566
-2.5	(-5/8, -5/8, -5/8, -5/8)	-16.095	2.991	3.595	6.586	-9.509	2.5	(5/8, 5/8, 5/8, 5/8)	43.627	7.017	2.494	9.511	53.138
	(-1, -1/2, -1/2, -1/2)	-15.919	0.494	5.962	6.456	-9.463		(1, 1/2, 1/2, 1/2)	43.685	3.354	6.068	9.422	53.107
	(-1, -3/4, -3/8, -3/8)	-15.844	-2.101	8.436	6.335	-9.509		(1, 3/4, 3/8, 3/8)	43.734	0.136	9.266	9.402	53.136
	(-1, -3/4, -2/4, -1/4)	-15.812	-2.242	8.691	6.449	-9.363		(1, 3/4, 2/4, 1/4)	43.746	-0.106	9.424	9.318	53.064
	(-1, -3/4, -3/4, 0)	-15.483	-6.518	12.820	6.302	-9.181		(1, 3/4, 3/4, 0)	43.925	-4.951	13.961	9.010	52.935
	(-1, -1, -1/4, -1/4)	-15.582	-7.584	13.887	6.303	-9.279		(1, 1, 1/4, 1/4)	43.845	-6.466	15.462	8.996	52.841
	(-1, -1, -1/2, 0)	-15.361	-9.125	15.295	6.170	-9.191		(1, 1, 1/2, 0)	43.973	-7.790	16.593	8.803	52.776
-3.0	(-3/4, -3/4, -3/4, -3/4)	-14.731	-2.788	9.788	7.000	-7.731	3.0	(3/4, 3/4, 3/4, 3/4)	56.420	0.058	10.219	10.277	66.697
	(-1, -2/3, -2/3, -2/3)	-14.627	-5.009	11.905	6.896	-7.731		(1, 2/3, 2/3, 2/3)	56.443	-1.905	12.109	10.204	66.647
	(-1, -1, -1/2, -1/2)	-14.425	-7.827	14.517	6.690	-7.735		(1, 1, 1/2, 1/2)	56.523	-6.657	16.577	9.920	66.443
	(-1, -1, -3/4, -1/4)	-14.301	-10.579	17.277	6.698	-7.603		(1, 1, 3/4, 1/4)	56.585	-9.340	19.149	9.809	66.394
	(-1, -1, -1, 0)	-13.748	-17.295	23.588	6.293	-7.455		(1, 1, 1, 0)	56.897	-17.628	26.698	9.070	65.967
-3.5	(-7/8, -7/8, -7/8, -7/8)	-11.595	-11.455	18.756	7.301	-4.294	3.5	(7/8, 7/8, 7/8, 7/8)	71.002	-10.902	21.286	10.384	81.386
	(-1, -5/6, -5/6, -5/6)	-11.566	-11.142	18.420	7.278	-4.288		(1, 5/6, 5/6, 5/6)	71.014	-10.676	21.261	10.585	81.599
	(-1, -1, -3/4, -3/4)	-11.501	-12.790	19.905	7.115	-4.386		(1, 1, 3/4, 3/4)	71.028	-12.365	22.870	10.505	81.533
	(-1, -1, -1, -1/2)	-11.322	-15.305	22.244	6.939	-4.383		(1, 1, 1, 1/2)	71.103	-15.514	25.758	10.244	81.347

TABLE I. The exchange E_x , the correlation E_c and the total E_{tot} energies of competing flavor-symmetry broken states, calculated using $\epsilon_{BN} = 5.1$. The lowest E_{tot} and E_{xc} are marked bold at each ν . On the electron-doped side, the ground state prefers flavor paramagnetism for $|\nu| < 1.0$ and flavor polarization for $|\nu| \geq 1.0$. On the hole-doped side, however, the ground state favors flavor paramagnetism for $|\nu| \leq 2.0$ and flavor polarization for $|\nu| \geq 2.0$. Energies are in the unit of meV per moiré unit cell. The kinetic energy E_k , defined as $E_k = E_{band} - 2E_H$ where E_{band} and E_H are the band energy and the Hartree energy of the SCH quasi-particle bands respectively, is regularized by the kinetic energy of flavor paramagnetic state at each filling ν .

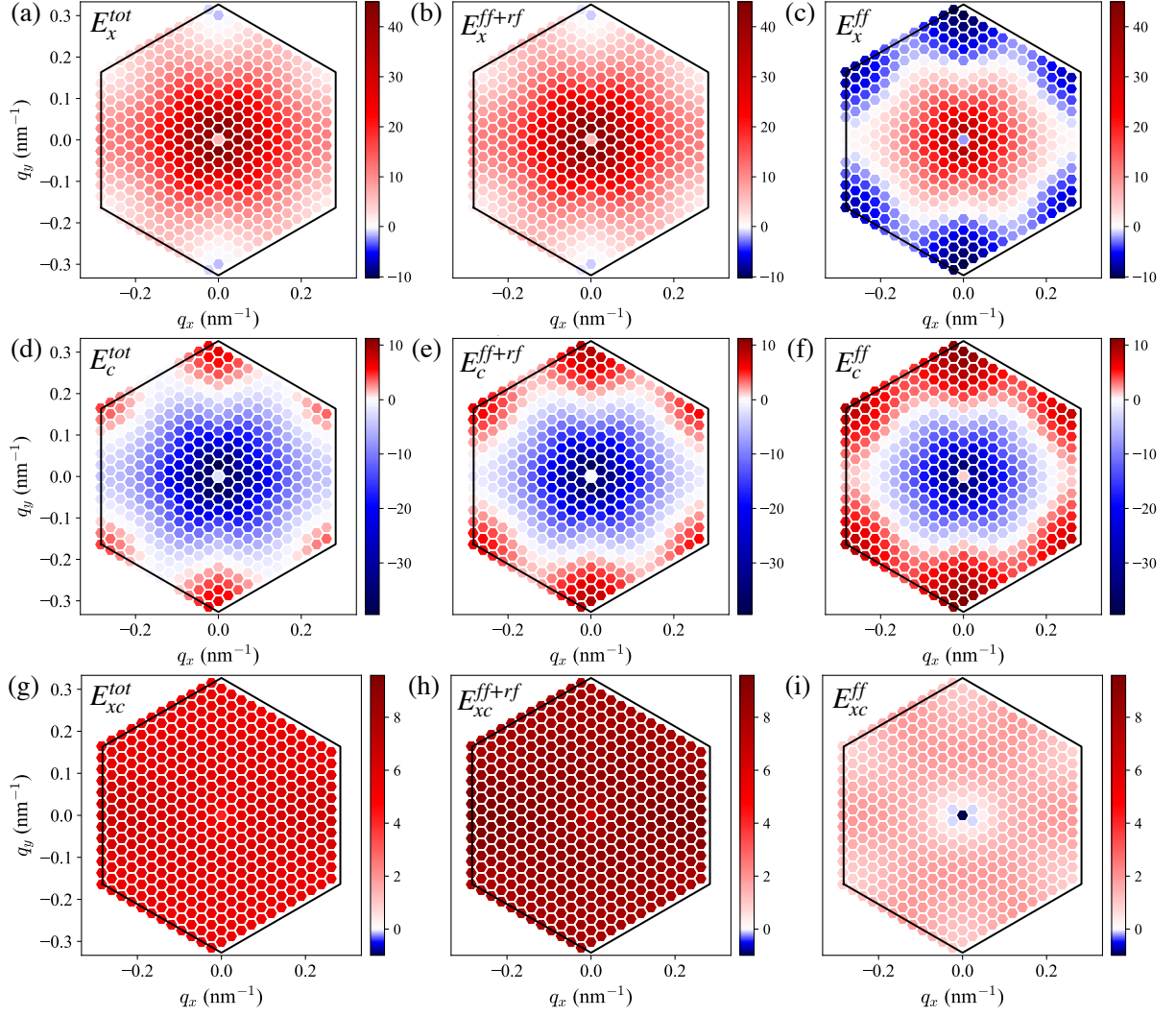


FIG. 11. Energies versus \mathbf{q} of the paramagnetic state at $\nu = -1$. (a-c) The exchange energy including excitations between all SCH bands (E_x^{tot}), between flat bands and between flat and remote bands (E_x^{ff+rf}), between flat bands only (E_x^{ff}). (d-f) The correlation energy. (g-i) The xc energy.

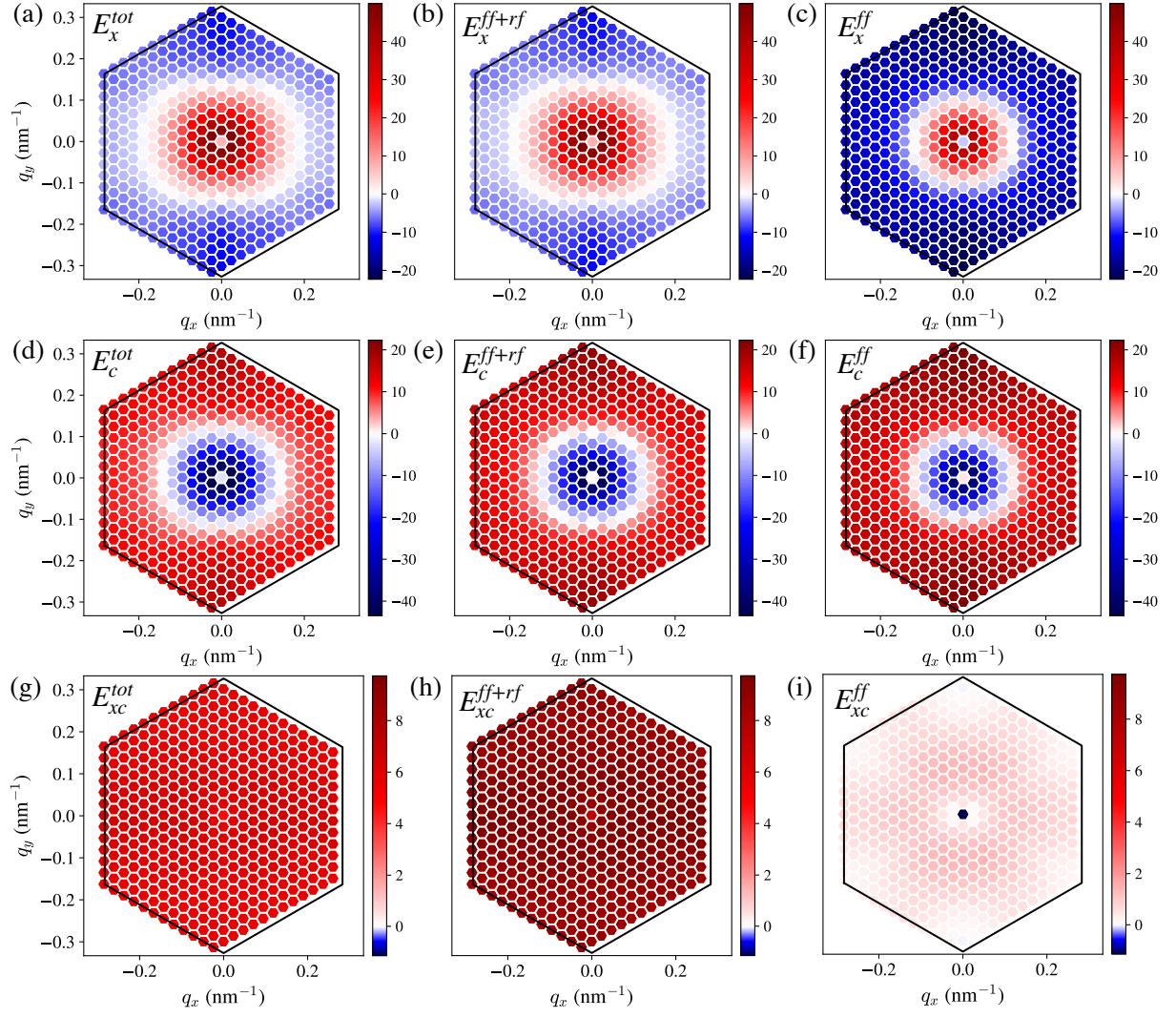


FIG. 12. Energies versus \mathbf{q} of the polarized state at $\nu = -1$.

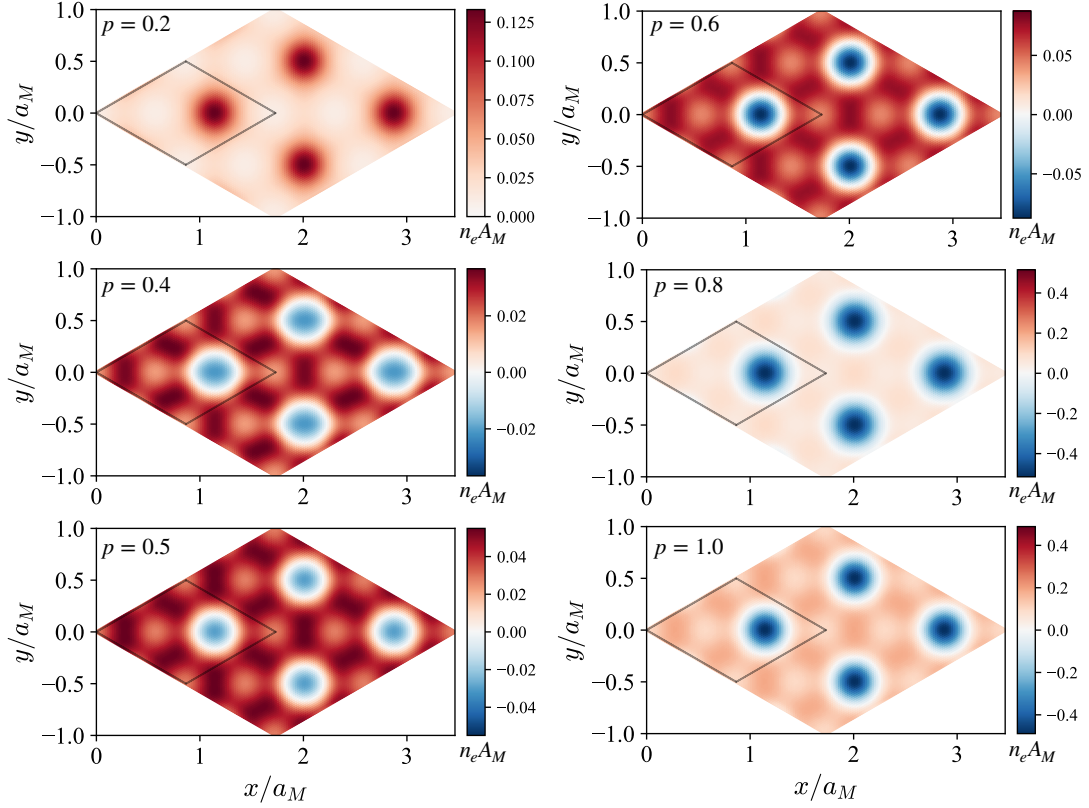


FIG. 13. Density distributions in real-space for $\nu = 0$, shown for various polarizations $p = 0.2, 0.4, 0.5, 0.6, 0.8, 1.0$. These correspond to Fig. 3(a) in the main text, where polarization p is defined. Displayed densities account for two flat band contributions and are depicted after subtraction of the $p = 0$ baseline. Compared to finite filling cases as shown in Fig. 14, densities for $\nu = 0$ are at least one order of magnitude smaller and therefore approximately uniform for all p . Density is in unit of $n_e A_M$, where A_M is the area of moiré unit cell. The grey rhombus outlines the moiré unit cell.

ν	$(\nu_1, \nu_2, \nu_3, \nu_4)$	E_0	E_x	E_c	E_{xc}	E_{tot}	ν	$(\nu_1, \nu_2, \nu_3, \nu_4)$	E_0	E_x	E_c	E_{xc}	E_{tot}
-1.0	$(-1/4, -1/4, -1/4, -1/4)$	-4.119	25.398	-21.363	4.034	-0.084	1.0	$(1/4, 1/4, 1/4, 1/4)$	19.664	30.622	-26.822	3.800	23.464
	$(-1/2, -1/4, -1/4, 0)$	-3.980	23.401	-19.643	3.758	-0.221		$(1/2, 1/4, 1/4, 0)$	19.785	25.797	-21.969	3.828	23.613
	$(-1/2, -1/2, 0, 0)$	-3.809	21.189	-17.977	3.212	-0.597		$(1/2, 1/2, 0, 0)$	19.749	20.717	-17.055	3.662	23.411
	$(-3/4, -1/4, 0, 0)$	-3.768	17.368	-14.212	3.156	-0.612		$(3/4, 1/4, 0, 0)$	19.697	16.836	-13.436	3.400	23.096
	$(-1, 0, 0, 0)$	-3.500	6.145	-4.249	1.897	-1.604		$(1, 0, 0, 0)$	19.796	4.637	-2.015	2.622	22.418
-2.0	$(-1/2, -1/2, -1/2, -1/2)$	-3.919	41.452	-34.390	7.062	3.143	2.0	$(1/2, 1/2, 1/2, 1/2)$	43.469	41.064	-33.315	7.749	51.218
	$(-1, -1/3, -1/3, -1/3)$	-3.787	30.464	-23.639	6.826	3.039		$(1, 1/3, 1/3, 1/3)$	43.534	28.905	-21.296	7.609	51.144
	$(-1, -1/2, -1/2, 0)$	-3.106	27.850	-21.761	6.089	2.983		$(1, 1/2, 1/2, 0)$	43.903	26.511	-19.296	7.215	51.118
	$(-1, -1, 0, 0)$	-2.244	14.628	-10.070	4.558	2.314		$(1, 1, 0, 0)$	44.375	12.460	-6.424	6.036	50.411
-3.0	$(-3/4, -3/4, -3/4, -3/4)$	2.155	47.234	-38.426	8.808	10.963	3.0	$(3/4, 3/4, 3/4, 3/4)$	72.566	45.210	-33.703	11.507	84.073
	$(-1, -2/3, -2/3, -2/3)$	2.118	43.554	-34.843	8.711	10.829		$(1, 2/3, 2/3, 2/3)$	72.541	41.623	-30.052	11.570	84.111
	$(-1, -1, -1/2, -1/2)$	2.134	36.756	-27.537	9.219	11.353		$(1, 1, 1/2, 1/2)$	72.583	35.136	-23.817	11.320	83.903
	$(-1, -1, -3/4, -1/4)$	2.270	34.094	-25.249	8.846	11.116		$(1, 1, 3/4, 1/4)$	72.710	32.033	-20.865	11.168	83.878
	$(-1, -1, -1, 0)$	3.562	26.476	-18.317	8.159	11.721		$(1, 1, 1, 0)$	73.749	22.621	-12.401	10.219	83.968

TABLE II. Same as in Table I but with broken C_2T by using a massive Dirac Hamiltonian in the BM model. The mass terms in top and bottom layers are both 10 meV.

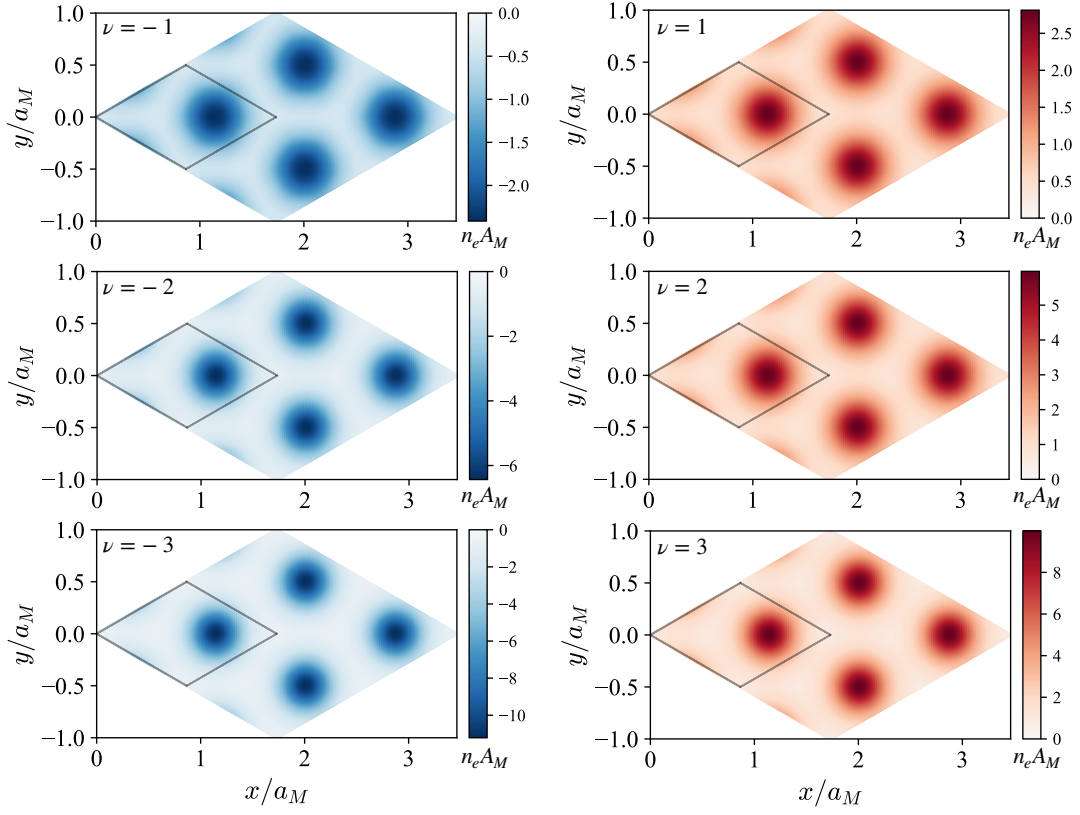


FIG. 14. Density distributions in real-space for the paramagnetic state, as a comparison to Fig. 13, displayed at different fillings $\nu = \pm 1, \pm 2, \pm 3$.

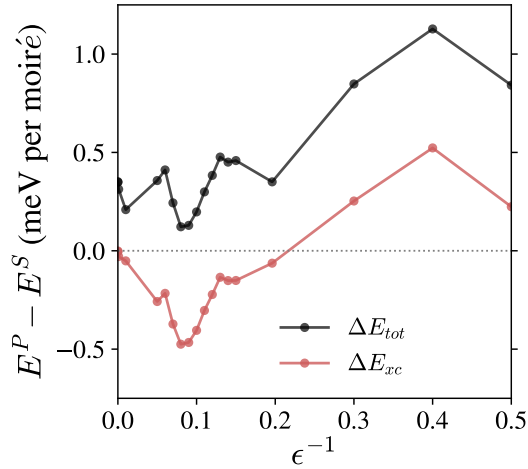


FIG. 15. The energy difference, defined as $\Delta E = E^P - E^S$, between flavor fully polarized state (P) and flavor paramagnetic state (S) at $\nu = -1$ as a function of Coulomb interaction strength ϵ^{-1} . ΔE_{tot} and ΔE_{xc} are energy difference of RPA total and xc energies respectively.